

University of New Hampshire

University of New Hampshire Scholars' Repository

Doctoral Dissertations

Student Scholarship

Winter 2010

Computational studies of nonlinear dispersive plasma systems

Xin Qian

University of New Hampshire, Durham

Follow this and additional works at: <https://scholars.unh.edu/dissertation>

Recommended Citation

Qian, Xin, "Computational studies of nonlinear dispersive plasma systems" (2010). *Doctoral Dissertations*. 545.

<https://scholars.unh.edu/dissertation/545>

This Dissertation is brought to you for free and open access by the Student Scholarship at University of New Hampshire Scholars' Repository. It has been accepted for inclusion in Doctoral Dissertations by an authorized administrator of University of New Hampshire Scholars' Repository. For more information, please contact Scholarly.Communication@unh.edu.

**COMPUTATIONAL STUDIES OF NONLINEAR
DISPERSIVE PLASMA SYSTEMS**

BY

Xin Qian

B.S. Wuhan University, 2000

M.S. Wuhan University, 2003

DISSERTATION

Submitted to the University of New Hampshire

In Partial Fulfillment of

The Requirements for the Degree of

Doctor of Philosophy

In

Physics

December, 2010

UMI Number: 3442540

All rights reserved

INFORMATION TO ALL USERS

The quality of this reproduction is dependent upon the quality of the copy submitted.

In the unlikely event that the author did not send a complete manuscript and there are missing pages, these will be noted. Also, if material had to be removed, a note will indicate the deletion.



UMI 3442540

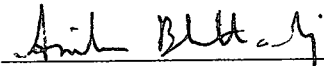
Copyright 2011 by ProQuest LLC.

All rights reserved. This edition of the work is protected against unauthorized copying under Title 17, United States Code.

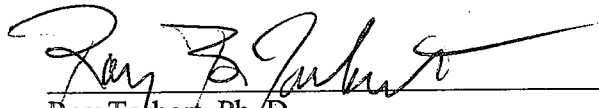


ProQuest LLC
789 East Eisenhower Parkway
P.O. Box 1346
Ann Arbor, MI 48106-1346

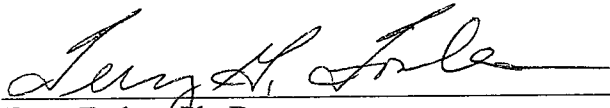
This dissertation has been examined and approved.



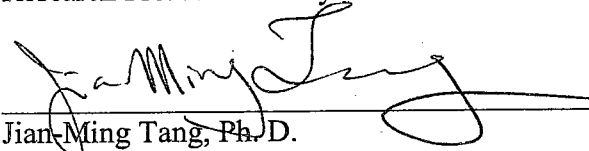
Amitava Bhattacharjee, Ph. D.
Dissertation Director, Professor of Physics



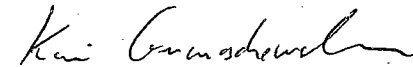
Roy Torbert, Ph. D.
Professor of Physics



Terry Forbes, Ph. D.
Research Professor of Physics



Jian-Ming Tang, Ph. D.
Assistant Professor of Physics



Kai Germaschewski, Ph. D.
Assistant Professor of Physics

12/10/2010

Date

ACKNOWLEDGEMENTS

This research would not have been possible without the support and encouragement of a great number of friends, family and colleagues.

I would like to express my gratitude to Prof. Amitava Bhattacharjee for the guidance and invaluable feedback he provided in supervising my thesis. I appreciate his patience and understanding over the past six years. His knowledge and wisdom has always been a constant source of inspiration.

This thesis is the culmination of many years of academic development, and along the way I benefited much from the guidance of truly wonderful scholars at New Hampshire and elsewhere. I would like to thank the other members of my committee, Prof. Roy Torbert, Terry Forbes, Jian-Ming Tang and Kai Germaschewski for the assistance they provided at all levels of the research. A very special thanks goes out to Professor Jorge Balbás. for his help on the numerical model in this study.

Finally, I would like to thank my family and friends for their love and encouragement. I am deeply indebted to them for the support they provided me through my entire PHD life in the U.S.

TABLE OF CONTENTS

ACKNOWLEDGEMENTS	iii
TABLE OF CONTENTS.....	iv
List of Figures	vi
ABSTRACT.....	x
Chapter 1 Conceptions and Background.....	1
1.1 Mach Cone in Dusty Plasma	1
1.2 Magnetic Reconnection.....	3
1.3 My Research Work	8
Chapter 2 3D Mach Cone in Dusty Plasma.....	11
2.1 Introduction.....	11
2.2 Numerical Method	13
2.3 3D Crystal Structure	17
2.4 3D Mach Cone.....	34
2.5 Conclusion	42
Chapter 3 Applying CentPACK TO HALL MHD simulations	43
3.1 Hall MHD Equation and Normalization.....	43
3.2 Applying Kurganov and Tadmor Central Schemes in Hall MHD	49
3.2.1 Central Schemes.....	49
3.2.2 Special Topics About the Hall MHD Simulation	54

3.3 The Dispersion Relationship Test	57
3.4 Hall MHD Reconnection Simulation	60
3.4.1 Initial condition and boundary condition	60
3.4.2 Hall MHD Reconnection with Hyper-Resistivity	63
3.5 Hall MHD simulations including electron inertia	69
3.6 Conclusion	74

References 76

List of Figures

Figure 2-1: Particle positions in the 3D space	23
Figure 2-2: Particle position in x, y coordinates in the $z = 0$ cut plane.....	23
Figure 2-3: Particle separation of the whole crystal in the $z = 0$ plane	24
Figure 2-4: Particle separation of the whole crystal in the $x = 0$ plane.....	25
Figure 2-5: Particle separation of the whole crystal in the $y = 0$ plane.....	26
Figure 2-6: 3D $g_{3D}(r)$ for the whole crystal in the 3D computational case	27
Figure 2-7: $g_{2D}(r)$ on the $z = 0$ plane in the 3D computational case.....	27
Figure 2-8: $G_4(r)$ on the $z = 0$ plane in the 3D computational case	28
Figure 2-9: $G_6(r)$ on the $z = 0$ plane in the 3D computational case	28
Figure 2-10: Count of the particles' neighbors in the 2D computational case.....	29
Figure 2-11: $g_{2D}(r)$ in the 2D computational case	29
Figure 2-12: $G_4(r)$ in the 2D computational case	30
Figure 2-13: $G_6(r)$ in the 2D computational case	30
Figure 2-14: Particles' position on the top surface (The color is particle separation)	31
Figure 2-15: Count of particles' neighbors on the top surface	31
Figure 2-16: $g_{2D}(r)$ on the top surface according to particles' x, y positions.....	32
Figure 2-17: $G_4(r)$ on the top surface according to particles' x, y position	32
Figure 2-18: $G_6(r)$ on the top surface according to particles' x, y position	33

Figure 2-19: Particle's positions in $z = 0$ plane for 500-particle system	33
Figure 2-20: 3D Mach cone in the ($ v $ (cm) in the $z = 0$ plane)	38
Figure 2-21: Mach cone in 3D system (3D figures).....	38
Figure 2-22: 3D Mach cone ($ v $ (cm) in the $x = 0$ plane)	38
Figure 2-23: 3D Mach cone (v_x in the $z = 0$ plane).....	38
Figure 2-24: 3D Mach cone ($ v $ (cm) in the $y = 0$ plane)	38
Figure 2-25: 3D Mach cone (v_x in the $z = 0$ plane), with apparent second wind.....	38
Figure 2-26: 3D Mach cone (v_y in the $z = 0$ plane).....	39
Figure 2-27: $ v $ in 2D system, produced by $f_0 = 1.56 \times 10^{-13} \text{ N}$	39
Figure 2-28: 3D Mach cone (v_z in the $z = 0$ plane)	39
Figure 2-29: Mach cone on the surface produced by $f_0 = 1.56 \times 10^{-13} \text{ N}$ $V_L = 1.65 \text{ cm/s}$	39
Figure 2-30: 3D Mach cone, $ v $ in $z = 0$ plane, produced by $f_0 = 1.56 \times 10^{-13} \text{ N}$	39
Figure 2-31: Mach cone on the surface produced by $f_0 = 1.56 \times 10^{-13} \text{ N}$ $V_L = 1.65 \text{ cm/s}$	39
Figure 2-32: Mach cone on the surface produced by $f_0 = 1.56 \times 10^{-13} \text{ N}$, $V_L = 13.2 \text{ cm/s}$	40
Figure 2-33: Side view of the Mach cone on the surface	40
Figure 2-34: Mach cone on the surface produced.....	40
Figure 2-35: Mach cone on the $7a$ deep layer under surface	40
Figure 2-36: $ v $ in the 2D system, produced by $f_0 = 1.56 \times 10^{-13} \text{ N}$ and $v = 270$	40
Figure 2-37: $ v $ in the 2D system, produced by $f_0 = 1.56 \times 10^{-13} \text{ N}$ and $v = 27$	40
Figure 2-38: $ v $ in the 2D system, produced by $f_0 = 1.56 \times 10^{-13} \text{ N}$ and $v = 2.7$	41

Figure 2-39: $ \nu $ in the 3D system, produced by $f_0 = 5 \times 10^{-13} N$ and $\nu = 314$	41
Figure 2-40: $ \nu $ in the 3D system, produced by $f_0 = 5 \times 10^{-13} N$ and $\nu = 31.4$	41
Figure 2-41: $ \nu $ in the 3D system, produced by $f_0 = 5 \times 10^{-13} N$ and $\nu = 3.14$	41
Figure 2-42: $ \nu $ in the 3D system, the Mach cone by perturbation on surface	41
Figure 2-43: $ \nu $ in the 3D system. the Mach cone by perturbation under surface.....	41
Figure 3-1: Dispersion relationship test result	60
Figure 3-2: Out of plane magnetic field at very beginning stage of the simulation	63
Figure 3-3: Reconnection rate for resistivity Hall MHD simulation	64
Figure 3-4: Current sheet's evolvement when reconnection rate is increasing gently	65
Figure 3-5: The current sheet shapes after quasi-steady state forms	65
Figure 3-6: Terms in generalized Ohm's law at $33.6\omega_i^{-1}$	67
Figure 3-7: Electron's outflow at $33.6\omega_i^{-1}$	68
Figure 3-8: Terms in generalized Ohm's law in diffusive region	69
Figure 3-9: Out of plane current density in case 1 at $14.4\omega_i^{-1}$	71
Figure 3-10: Out of plane current density in case 1 at $16.1\omega_i^{-1}$	71
Figure 3-11: Reconnection rate for case 1.....	71
Figure 3-12: Out of plane current density in case 2 at $14.0\omega_i^{-1}$	72
Figure 3-13: Out of plane current density in case 2 at $19.4\omega_i^{-1}$	72
Figure 3-14: Reconnection rate for case 2.....	72
Figure 3-15: Out of plane current density in case 3 at $13.1\omega_i^{-1}$	73

Figure 3-16: Out of plane current density in case 3 at $14.8 \omega_i^{-1}$	73
Figure 3-17: Reconnection rate in case 3	73
Figure 3-18: Out of plane current density in case 4 at $14.2 \omega_i^{-1}$	73
Figure 3-19: Out of plane current density in case 4 at $17.6 \omega_i^{-1}$	73
Figure 3-20: Reconnection rate in case 4	73

ABSTRACT

COMPUTATIONAL STUDIES OF NONLINEAR DISPERSIVE PLASMA SYSTEMS

BY

Xin Qian

University of New Hampshire, Dec, 2010

Plasma systems with dispersive waves are ubiquitous. Dispersive waves have the property that their wave velocity depends on the wave number of the wave. These waves show up in weakly as well as strongly coupled plasmas, and play a significant role in the underlying plasma dynamics. Dispersive waves bring new challenges to the computer simulation of nonlinear phenomena. The goal of this thesis is to discuss two computational studies of plasma phenomena, one drawn from strongly coupled complex or dusty plasmas, and the other from weakly coupled hydrogen plasmas.

In the realm of dusty plasmas, we focus on the problem of three-dimensional (3D) Mach cones which we study by means of Molecular Dynamics (MD) simulations, assuming that the dust particles interact via a Yukawa potential. While laboratory and MD simulations have explored thoroughly the properties of Mach cones in 2D, elucidating the important role of dispersive waves in the formation of multiple cones, the simulations presented in this thesis represent the first 3D MD studies of Mach cones in strongly coupled dusty plasmas. These results have qualitative similarities with experimental observations on 3D Mach cones from the PK-3 plus project, which studies complex plasmas under microgravity conditions aboard the International Space station.

In the realm of weakly coupled plasmas, we present results on the application of non-oscillatory central schemes to Hall MHD reconnection problems, in which the presence of dispersive whistler waves presents a formidable challenge for numerical algorithms that rely on explicit time-stepping schemes. In particular, we focus on the semi-discrete central formulation of Kurganov and Tadmor (2000), which has the advantage that it allow for larger time steps, and with significantly smaller numerical viscosity, than fully discrete schemes. We implement the Hall MHD equations through the CentPACK software package that implements the Kurganov-Tadmor formulation for a wide range of hyperbolic problems, thus adding to the toolkit of applications accessible to the users of CentPACK. Our particular application focuses on Hall MHD reconnection in the presence of resistivity, electron inertia, and hyperresistivity as mechanisms that break field lines. For simulations of modest system size of the type presented in this thesis, all of these mechanisms exhibit rapid impulsive onset with X-point geometry.

CHAPTER 1

CONCEPTIONS AND BACKGROUND

In this thesis, I discuss our computational study on nonlinear dispersive plasma systems. In this chapter, I introduce the two physical problems that I have studied and provide some background. In chapter 2, I discuss molecular dynamics simulations of 3D Mach cones in dusty (or complex) plasma, including the formation of multiple Mach cones, supported by dispersive waves. In chapter 3, I introduce a new numerical method for Hall MHD simulations of magnetic reconnection in which dispersive whistler waves play an important role. In chapter 4, I present my Hall MHD reconnection simulation results using this new numerical method.

1.1 Mach Cone in Dusty Plasma

Dispersive waves not only bring challenges to the computer simulation of the nonlinear phenomena, they also provide some benefits. As for the strongly coupled plasma or dusty plasma, the nature of dispersive waves can make the Mach cones have multiple Mach cone patterns, which have been demonstrated convincingly in two dimensions. The multiple cone patterns within dusty plasma can disclose many features of the dusty plasma, and can act as a diagnostic tool for scientists.

Dusty plasmas or complex plasma systems are formed by dusty particles [*Dubin and O'Neil*, 1999; *Ma and Bhattacharjee*, 2002; *Mann*, 2008; *Shukla*, 2001; *Verheest*, 1996]. These particles have been observed to interact with each other via the Yukawa

potential in 2D systems [Konopka *et al.*, 2000]. The coupling of dusty plasma is measured by the parameter $\Gamma = Q^2 / 4\pi\epsilon_0 akT$, where Q is the charge of the particles, a is the average distance between the particles, and T is the temperature of the particles. Γ is just the ratio between the potential energy and the kinetic energy of the dust particles. Parameter Γ is very large ($\Gamma \gg 1$) in dusty plasma. Therefore, dusty plasma is categorized as strongly coupled. Standard plasmas in the laboratory and space have small Γ , which is called a weakly coupled plasma. These weakly coupled plasmas are in gaseous state. Strongly coupled plasmas, on the other hand, are usually in solid or liquid state.

Several space exploration projects are currently examining or going to examine the dusty environment in space. The Cassini project is providing insight into the dusty plasma environment on Saturn [Havnes *et al.*, 1996; Horányi *et al.*, 2004; Wahlund *et al.*, 2009]. A scientific goal of the Solar Probe mission is to “explore dusty plasma phenomena near the Sun and its influence on the solar wind and energetic particle formation”. The PK-3 Plus project is for the dusty plasma experiment under the micro-gravity condition on the International Space Station (ISS) [Thomas *and et al.*, 2008].

Experimental studies in air show that a Mach cone is formed by the interaction of wave fronts which are excited by a perturbation moving faster than the acoustic wave in matter. The Mach cone is the region inside the shock. The Mach cone in a dusty plasma can be excited by charged particles or by a laser spot moving at supersonic speed. Waves contained within dusty plasma have broadly two types, as follows [Peeters and Wu, 1987]: shearing waves and compressional waves. Therefore, Mach cones in dusty plasma also have two categories, which correspond either to shearing waves or compressional

waves, although both kinds of Mach cones can be produced simultaneously [*Havnes et al.*, 1995; *Havnes et al.*, 1996].

Mach cones are a very important diagnostic tool for the dusty plasma environment [*Havnes et al.*, 1996]. 2D Mach cones have been studied fairly well. The work presented in this thesis focuses on 3D Mach cones---their existence, under the conditions under which they form.

In addition to the waves contained within dusty plasma, researchers are also interested in the phase transition process within dusty plasma between crystalline and liquid states. Since particle motions in the dusty plasma system can be observed in detail [*Morfill and Thomas*, 1996; *Schweigert et al.*, 2000], dusty plasma is a good matrix for studying the phase transition process.

The dispersive nature of the waves in dusty plasma can influence the wave patterns of Mach cones. Waves with different wave lengths can be superimpose coherently to form multiple Mach cones, a consequence of the dispersive waves in the system. Dubin [*Daniel H. E*, 2001] provided an analysis for 2D Mach cones in strongly coupled dusty plasma. No such definitive theories exist for either the wave spectrum or Mach cones in 3D dusty plasmas. Therefore, in this thesis we focus on simulations.

1.2 Magnetic Reconnection

Besides shock, magnetic reconnection is another irreversible process in space and laboratory plasmas, during which magnetic energy is quickly converted into kinetic and thermal energy. At the reconnection site, which is the diffusive region, the magnetic frozen-in condition is broken. There are two perspectives for research in this area. One is

how one should model the reconnection process itself, and the other is how this process influences global space phenomenon. As for the first topic, the main puzzle is why the reconnection rate is higher than the predictions of classical resistive MHD theory, discussed for instance in basic textbooks [*Gurnett and Bhattacharjee, 2005*]. How the magnetic reconnection influences global space phenomenon includes how the particles, especially the electrons, are accelerated by the reconnection process, and the actual role of the magnetic reconnection during eruptive events such as CME (Coronal Mass Ejection) and magnetic substorms. Our research focused on the first perspective.

The Sweet-Parker model is a classic MHD model for reconnection. The model indicates that the reconnection rate has a scaling of $S^{-1/2}$. Here S is the Lundquist number. The Lundquist number is a dimensionless ratio of time that an Alfvén wave crosses a length scale to a time that the magnetic field diffuses in the same length scale. The lower resistivity and larger length scale will cause the larger the Lundquist number. Usually Lundquist number is very large in collisionless plasma. So for the collisionless space plasma phenomenon, the Sweet-Parker model always predicts a very low reconnection rate, which cannot be supported by observations.

Petschek proposed another mode which includes the slow shock and the MHD wave in the MHD model [*Petschek, 1964*]. Petschek's model claimed to solve two outstanding problems of magnetic reconnection. The short current sheet in Petschek model can predict the high reconnection rate, or to say the fast magnetic topology changing. Petschek model also states that the plasma acceleration not only happens in the diffusion region but also on slow shocks in Petschek's model. The second point relates to how energy is converted within the reconnection process. Petschek's model was

the first widely accepted reconnection model. However, after computer simulations became popular in the 1980s, researchers found that the Petschek model was not realizable in computer simulations in the high-Lundquist-number regime except in circumstance when non-uniform resistivity was imposed. Thus they doubt the validity of the model itself.

Biskamp and other researchers [*D. Biskamp et al.*, 1995; *Ma and Bhattacharjee*, 1996; *Shay et al.*, 1999] proposed that the Hall effect may limit the current length and enable a high reconnection rate within the MHD model. The Hall effect is caused by the physical fact that an ion is much heavier than an electron, which can be important when the current sheet width drops into the ion inertia scale range. In addition to simulations, both in-situ space observations [*Deng and Matsumoto*, 2001] and laboratory experiments [*Ren et al.*, 2005] provide evidence that the Hall effect plays an important role during the reconnection process. Hall MHD reconnection simulations indicate that with the same macroscopic parameters (including the plasma β , the boundary conditions, etc.), the reconnection rate is a constant value independent of the resistivity. Although researchers agree that the GEM challenge proves that different physical numerical models including particle-in-cell (PIC), hybrid, and Hall MHD provide the same (high) reconnection rates when the Hall effect has been included in the numerical model, it does not resolve conclusively the issue of why high reconnection rates can occur. The high reconnection rate within the PIC simulation may not be caused by the Hall effect, and how energy is transferred and apportioned between electrons and ions.

Recent PIC simulations show that electron-positron plasmas could also have a fast reconnection process [*Bessho and Bhattacharjee*, 2007] without the Hall effect. Open

boundary or large system size PIC simulations show long current sheets within the approximate 5-10 ion inertial range [Daughton *et al.*, 2006; Fujimoto, 2006; Karimabadi *et al.*, 2007] within the fast magnetic reconnection process, while classic Hall MHD simulations always provide a singular current sheet with X-point geometry. PIC simulations raise questions regarding the Hall MHD model. The high reconnection rate is not necessarily associated with a short current sheet in high S plasma, which is established by Sweet-Parker theory, and can be easily proved by MHD theory. The Hall effect is not necessary to cause the high reconnection rate, or it is not the only reason for high reconnection rate, because without it, high reconnection rate is also realizable. These PIC simulations suggest that the collisionless effect or the kinetic effect is the key for the high reconnection rate and energy conversion.

The above research work are all following the conclusion that the classic resistivity MHD model is not adequate for describing magnetic reconnection in collisionless plasma, as suggested by the Sweet-Parker model [Bhattacharjee *et al.*, 2009]. However, recent theoretical work suggests that plasmoid instability [Loureiro *et al.*, 2007] has a linear growth rate, γ , of $S^{1/4}(V_A/L)$. The prediction suggests that with only the resistivity MHD for a high S plasma, a high reconnection is also possible. Bhattacharjee and his colleagues investigate this instability numerically and analytically in the nonlinear regime [Bhattacharjee *et al.*, 2009; Huang and Bhattacharjee, 2010; Huang *et al.*, 2010]. These works as well as other researchers recent research works [Daughton *et al.*, 2009; Loureiro *et al.*, 2009; Samtaney *et al.*, 2009; Shepherd and Cassak, 2010] should change people's view point on the magnetic reconnection problem. Further details can be found in Figure 1 in reference [Huang *et al.*, 2010].

One of the primary questions that drove the present investigations is whether Hall MHD simulations that include finite particle inertia can produce extended current sheets and secondary instabilities of the type seen in recent PIC simulations. There was an indication in the work of [Ma and Bhattacharjee, 1999] that this might be so. In those simulations, some extension of the thin current sheet was seen, interrupted by a secondary instability. Reduced four-field equations, on the other hand, produced a cusp like structure in the diffusion region. Since the numerical implementation of the electron inertia term is very different in the above simulations, we were interested in investigating the various numerical implementations of the electron inertia term within the Hall MHD simulation.

The role of dispersive waves, or more specifically the whistler wave in the Hall MHD system, is another interesting issue in the magnetic reconnection process. Many researchers believe that dispersive waves play an important role in the dynamics. Space in-situ observations have also confirmed the whistle wave's existence near the diffusion region [Deng *et al.*, 2009]. After the Hall MHD model was proposed, there was a long-term controversial discussion concerning the role of the whistler wave in the magnetic reconnection process. Now it is widely accepted that the Hall effect will squeeze the current sheet length in the reconnection process. Furthermore, some researchers have proposed that it is the whistler like dispersion relationship of the waves within the Hall MHD that squeezes the current length and the short current sheet in Hall MHD simulation, causing the high reconnection rate in the electron-proton plasma. The second statement has been questioned by large scale or open boundary PIC simulations and electron-positron reconnection simulations, since these simulations have a high

reconnection rate and long current sheets. As for the dispersion relationship, after electron inertia has been added to the Hall MHD simulation, the wave speed does not always increase with the wave number. For our simulations, Hall MHD has been run with various forms of electron inertia, and none showed current sheet elongation or secondary instability. The results are in agreement with our initial hypothesis that the current sheet length is not determined by a linear wave dispersion relationship.

Besides the dispersive wave's physics role, it also poses significant challenges in numerical simulation. In the Hall MHD, the wave speed will increase with the wave number. Reconnection simulation requires tiny space grids to represent the thin current sheet. This also requires tiny time steps to meet the CFL condition, which makes Hall MHD reconnection simulations very expensive. The Hall MHD reconnection simulation also needs very restricted numerical dissipation level to simulate the collisionless effect, while the tiny time step tends to cause large viscosity. Therefore, we were also interested in having a numerical method that can handle these numerical challenges.

1.3 My Research Work

As for the Mach cone in dusty plasmas, the goal of our research was to reveal the 3D Mach cone's basic properties in the dusty plasma crystal. New simulations for Mach cones in three-dimensional (3D) Yukawa crystals excited by external laser forcing were conducted. We first used a variation of a time relaxation method in order to achieve a static crystal system, in which particles were crystallized into the 3D Yukawa crystal. Then a moving laser perturbation spot is added to the system. In the resulting crystal-like system from the first step, no regular large lattice structures were observed in the inner

part of the system, while regular large lattices were observed on the surface. When a laser-like perturbation was added, it was found that under a variety of conditions, stable 3D Mach cones with multiple cone structure appear in the simulation. For the multiple layer structure near the surface, which has regular lattice, a similar perturbation does not produce multiple a Mach cone pattern.

For the Hall MHD reconnection phenomena, we focused on the numerical method. Based upon the physical background and the numerical challenge discussed above, I applied the CentPACK hyperbolic numerical package to the Hall MHD simulation with electron inertia. For an explicit numerical scheme, this did not highly reduce the computational resources consumed. However, the numerical viscosity in this numerical scheme did not increase when the time steps became small. Therefore, it satisfied the second numerical challenge within in Hall MHD simulation, and in the future can be used to handle the Hall MHD reconnection problem.

This numerical strategy decouples the numerical scheme and the physical equations. It will be easy for the physicists to utilize the new parallelization techniques. We only applied the MPI method in our simulation work. The new GPU parallel method has not been include in this thesis work, while it is also a very worthy approach. Besides decoupling the numerical scheme and the physical problem, the other way to go is still using more complex numerical schemes, but preparing some code generation methods for the physicists to simplify their programming work.

We used this new numerical method in the resistive Hall MHD simulation, and carefully examined the results by comparing them with other published results. The Hall MHD simulation and the dispersion relationship test confirmed the numerical method's

validity in both the linear and the nonlinear regime. Here, we have also included different forms of the electron inertia term within the Hall MHD simulation.

CHAPTER 2

3D MACH CONE IN DUSTY PLASMA

2.1 Introduction

Experiments, numerical simulations, and analytic research indicates that in a 2D dusty plasma, composed of a mono-layer of dusty particles, multiple V-shape Mach cones can be produced [*Dubin, 2000; Ma and Bhattacharjee, 2002; Samsonov et al., 1999*]. The corresponding situation in 3D is much less clear, both from the point of view of the structure of 3D dusty plasma crystals, as well as the existence of stable dispersive waves that are widely believed to support these Mach cones in 2D. The main result of this chapter is to demonstrate for the first time by means of 3D molecular dynamics simulations that multiple Mach cones can form in 3D crystals, supported by stable 3D dispersive waves, although the precise and complete dispersion relations of all the 3D waves are not known at the present time.

Preliminary 3D experiments have been performed for 3D dusty plasma [*Chu and I, 1994; Pieper et al., 1996*] which indicate that the multiple-layer structure can form fcc-/bcc-/hex-layers crystals in various situations. Some experiments and simulations have not determined a regular lattice within 3D dusty plasma [*Chen et al., 2005; Totsuji et al., 2005*], as we have found. On the surface of a 3D dusty plasma crystal, large regular lattices have been observed in experiments and simulations [*Dubin and O'Neil, 1999; Schiffer, 2002*]. In systems with few particles (around or under 10,000), multiple spherical plasma crystals can clearly be observed [*Dubin and O'Neil, 1999; Kahlert and*

Bonitz, 2010; Schiffer, 2002; Totsuji et al., 2005]. Regarding the wave mode, no reliable analysis of the mode dynamics of 3D dusty plasma has been possible thus far, although one experimental study indicates that large-scale low-frequency shear-like modes dominate this system [*Ivanov et al., 2009; Kahlert and Bonitz, 2010*]. Whereas in a 2D dusty plasma crystal, the complete wave spectrum has been predicted by Wang and Bhattacharjee [*Wang et al., 2001*], and tested by careful laboratory experiments [*Nosenko et al., 2002*], no such comprehensive studies exist in 3D.

Since Mach cones can be used as a diagnostic tool for plasma properties [*Havnes et al., 1996*] and have been pursued in space science in the context of Saturn's rings, it is interesting to understand how Mach cones behave in a 3D dusty plasma. Some 3D Mach cones experiment have now been done via the PK-3 plus project in International Space Station. A fluid simulation study has been done of this phenomenon [*Jiang et al., 2009*]. Our study is the first molecular dynamics simulation of this phenomenon, carried out with a large number of particles (90,000 particles). The work presented here is carried in the following steps: 1) The 2D numerical model is extended to 3D. 2) The crystal formation process is simulated, and the relevant structure function analysis is carried out. 3) Simulations of laser spots imposed onto 3D Yukawa crystals in order to excite Mach cones are presented. The number of particles in our study is at least one order of magnitude larger than other numerical studies performed in this field. Therefore, our numerical study reveals results not seen before, such as a clear separation of structure between the volume and surface regions, and the preferential formation of multiple Mach cones within the volume over the surface region.

2.2 Numerical Method

Our computational work consisted of two stages. The first stage includes cooling the particles with damping, so that they crystallize to form a 3D Yukawa crystal. The second stage adds a moving laser spot focused on the system to test whether multiple Mach cones pattern can be produced in the 3D crystal.

The numerical code developed for this study utilized a parallel Molecular Dynamic (MD) simulation algorithm. The governing equations are, as follows:

$$\frac{d^2 \mathbf{r}_i}{dt^2} = -\nabla \phi_i - mv \frac{d\mathbf{r}_i}{dt} + \mathbf{F}_L \quad (2.1)$$

$$\phi_i = k_x r_{xi}^2 + k_y r_{yi}^2 + k_z r_{zi}^2 - \sum_{i \neq j}^N \frac{Q^2}{4\pi\epsilon_0 r_{ij}} e^{-\frac{r_{ij}}{\lambda_D}} \quad (2.2)$$

$$\mathbf{F}_L = -f_0 e^{-\left(\frac{(x-V_L t)^2}{b_x^2} + \frac{y^2}{b_y^2} + \frac{z^2}{b_z^2}\right)} \hat{\mathbf{x}} \quad (2.3)$$

In these equations, the subscripts i and j represent the index of the particles. In equation (2.1), the term $mv \, d\mathbf{r}_i/dt$ is the Epstein damping force, and the term \mathbf{F}_L is the external laser force effect, whose detailed form is expressed in equation (2.3). The term ϕ_i is the potential energy of particle i . The terms containing $k_\alpha r_{\alpha i}^2$ in equation (2.2) express the confining force; here r_{xi}, r_{yi}, r_{zi} are the x, y, z components of \mathbf{r}_i ; and the terms containing k_x, k_y, k_z indicate that the harmonic confining electrostatic forces vary in the x, y, z directions. Term Q is the charge of the particles, which is the same for all particles. The last term in equation (2.2), which is the Yukawa potential term, indicates the interaction potential among the particles. In equation (2.2), x, y and z are the positions of particle

i , which are also the \hat{x} , \hat{y} and \hat{z} component of \mathbf{r}_i . The b_x , b_y and b_z parameters determine how large the laser spot is, and the parameter v_L is the speed of the laser spot along the \hat{x} direction.

The numerical method is based on the work of Ma and Bhattacharjee [*Ma and Bhattacharjee, 2002*]. The difference between the physical model here and the model in the work of Ma and Bhattacharjee is that the Yukawa potential has been extended to 3D. In addition to the Yukawa potential in 2D space, in the 2D simulation work the movement of dust particles is limited to the disk, while in 3D simulation work, particles can move in any direction within 3D space. In the 2D simulation, the direction of the confining force is contained within the horizontal disk. In 3D, the confining force is not only in the horizontal plane, but also has a vertical component.

In our 3D simulation, there are 90,000 particles. The number of particles was chosen such that the number is large enough to make the system amenable to many-body statistical mechanics concepts, as well as to attenuate the surface effect [*Dubin and O'eil, 1999*], and not too large so as to keep the CPU demands for the simulation relatively modest.

The confining force was chosen to be $k_x = k_y = k_z/10 = k_0$. Such an anisotropic confining force can make dusty particles form an oblate spherical system that can cover a larger area in the x, y plane than an isotropic confining force with the same particle number. Thus, in the perturbation stage, the laser spot has a larger movement range in the x, y plane.

The time derivatives in equation (2.1) above have been discretized. A second-order leap-frog scheme is utilized for the time-discretization. For equation (2.2), the distance between each particle is calculated. We set a threshold distance of $10\lambda_D$ under which we take into account the Yukawa interaction of the particles. Particles that are separated by a distance larger than this threshold are ignored when calculating the sum of the Yukawa potential from other particles. Since a central potential is used to confine the particles, an open boundary condition is applied.

When performing parallel computations, every node records a group of particle velocities, and all of the particle positions. After each step, every particle position is passed to each node in order to calculate the particles' new position within the subsequent time step. The algorithm here has a time complexity of $O(n^2)$. The computation time increases as a square function when the particle number increases. Computational geometry algorithms can be used to make the computations more efficient. However, the current algorithm is sufficient for doing the computation on a cluster with more than 40 processors within 2-3 days.

Typical parameters chosen in 2D and 3D simulations are presented in Table 2-1. From the table, one can determine that approximately 10 times the confining force parameter, k_0 , should be used in a 3D simulation than in a 2D simulation, to ensure similar particle separations within both systems. In this work, particle separation is not calculated as the Wigner-Seitz radius, but as the first radial peak of the pair correlation function, which in most cases is the same as the average of the "nearest layer neighbor distance" [Quinn and Goree, 2000].

Case	Particle Numbers	Q	λ_D (Debye Length)	m (Mass of Particle)	v	k_0	$\kappa = a/\lambda_D$ (a - Particle Separation)
3D	90,000	16,000e	526 μm	4.56 $\times 10^{-13}$ kg	3.14s $^{-1}$	1.9 $\times 10^{-12}$ kg/s 2	1.1
2D	5,000	15,700e	526 μm	5.2 $\times 10^{-13}$ kg	2.70s $^{-1}$	2.4 $\times 10^{-12}$ kg/s 2	1.3

Table 2-1: Physical Parameter Choices

In the initial crystal forming stage, the initial velocity distribution is chosen as Gaussian distribution. The positions of the particles are equally distributed in a $1cm \times 1cm \times 1cm$ cube. In this stage, the perturbation force amplitude, f_0 , is taken to be zero. In general, after 0.8s in physical time, using the parameters presented in Table 2-1, the system composed of dusty particles formed a structured system within the simulation domain. These particles constitute a strongly coupled system in the crystal or liquid state. Then, after approximately 10s in physical time, the $\langle |v| \rangle$ of the particles approach a low magnitude of $10^{-3} cm/s$. For this type of cooled dusty plasmas, the coupling parameter Γ , which is the ratio of the average Coulomb potential energy and the average kinetic energy, can be of the order of 10^6 . (In contrast, in weakly coupled plasmas, we typically have $\Gamma \ll 1$.) We choose this strongly coupled plasma as the initial condition on which laser forcing is imposed. In the perturbation stage, the perturbation force amplitude f_0 is non-zero. The perturbation laser spot moves in the positive x direction along the $z=0$ and the $y=0$ line.

2.3 3D Crystal Structure

In 2D experiments and simulations, the dusty plasma crystal always displays a regular hexagonal (hex) lattice with some defects [Ma and Bhattacharjee, 2002; Morfill and Thomas, 1996]. Several years ago, 3D experiments relating to crystal structures were performed that indicate that fcc-/bcc-/hex-layers crystals can form in various situations [Chu and I, 1994; Pieper et al., 1996]. Our work, consistent with some other studies, show that no regular structure is formed in the internal part of large 3D systems [Arp et al., 2004]; [Chen et al., 2005; Totsuji et al., 2005]. In contrast, we find that regular lattices can be found on the surface of crystals. With previous publications [auml et al., 2010; Dubin and O'eil, 1999; Ivanov et al., 2009; Schiffer, 2002], we think that the above result is caused by the so-called finite system-size effect. The 3D experimental studies conducted in the 1990s should be regarded more as multiple-layer small system-size experiments, instead of fully 3D experiments with a clear separation between surface and volume. For the simulation work presented here, we have used 90,000 particles, a number much larger than the particle number used in other studies (they used roughly, or less than 10,000 particles).

By examining the 3D volume and surface structures, the following inferences can be made: 1) If the system's particle number increases to a certain level [Schiffer, 2002], the volume characteristics of the system will manifest themselves, clearly separated from the surface structure. No pure lattice structure can be seen in the center of the dusty plasma system. 2) On the surface of dusty plasma, we find a regular lattice-structure, which we have explained as a finite-size effect above. 3) For a system with fewer than

1000 particles, a multiple shell structure can be found, with a regular lattice structure on each shell.

In this thesis, the crystal forming process is not discussed in detail because our primary focus is on Mach cones. Here, I provide details of the final snapshot of the crystal forming stage calculation and some of the structural analyses for this final snapshot.

In our typical simulation case, the particles' positions in 3D space and in the $z = 0$ plane are shown in Figure 2-1 and Figure 2-2. Finding a regular periodic lattice in the system is not easy. From Figure 2-3, Figure 2-4 and Figure 2-5 we determined that particle separation increases toward the outside of the crystal, a situation that can be found in 2D computational cases. The pictures also provide a brief idea about the system that we get in the crystallization stage, which is also the initial condition for the laser perturbation stage.

As for the surface, from Figure 2-14, which displays the particles' neighboring counts, one can see that except for some defects on the surface most of the particles on the surface have six neighbors, the same as for the 2D system. By comparing the 2D crystal structure (Figure 2-10), one can determine that the surface should also have a regular lattice. Such a result should be evidence that the regular lattices in previous 3D experiments are a product of a surface effect. The particles' neighbors are counted, from computational geometry using the Delaunay triangulation algorithm.

Correlation functions can provide normalized statistical analyses regarding a particles' position or the bonds between particles. These functions work very well for

characterizing 2D dusty plasma systems [Hua *et al.*, 2003; Quinn *et al.*, 1996]. In this research, we seek to expand these correlation function analyses to 3D.

The pair correlation function is used to measure the probability of finding two particles separated by a distance r . In this paper, for the 2D analysis, the pair correlation function uses the same form as Hua *et al.* [2003], in the forms of equation (2.4) and (2.6). For the 3D analysis, the pair correlation function is defined as equation (2.4) and (2.5). Equation (2.5) describes how many particles surround a certain particle with a distance as r varies. In equation (2.5), V/N is a normalization coefficient, where V is the volume size of the 3D analysis region and N is the total number of particles. The term V/N is, in fact, the volume density of the particle number. The term $N(r, \Delta)$ indicates the total number of particles within the shell with a radius between $r - \Delta/2$ and $r + \Delta/2$. The term $4\pi \cdot r^2 \Delta$ indicates the volume size of the shell. After function $g_{3D}^i(r)$ has been calculated for every particle in a certain region, $g_{nD}(r)$ is just the statistically expected value within this region, calculated using equation (2.4), as follows:

$$g_{nD}(r) = \frac{\sum_{i=1}^N g_{nD}^i(r)}{N} \quad (2.4)$$

$$g_{3D}^i(r) = \left(\frac{V}{N} \right) \frac{N(r, \Delta)}{4\pi \cdot r^2 \Delta} \quad (2.5)$$

$$g_{2D}^i(r) = \left(\frac{V}{N} \right) \frac{N(r, \Delta)}{2\pi \cdot r \Delta} \quad (2.6)$$

The bond-orientation correlation functions $G_6(r)$ and $G_4(r)$ are used to measure the orientational order of the system's structure in the 2D plane. Details of these equations

are found in references [Hua *et al.*, 2003; Pieper *et al.*, 1996; Quinn *et al.*, 1996]. In the pair correlation function, i indicates the particles. The statistical average is also performed for all of the particles in the system. For the bond-orientation correlation function, i indicates bonds. The statistical average is also determined using all of the bonds in the region. We define:

$$G_N(r) = \frac{\sum_{i=1}^N G_N^i(r)}{N} \quad (2.7)$$

$$G_6^i(r) = \cos(6 \cdot [\theta(r) - \theta(0)]) \quad (2.8)$$

$$G_4^i(r) = \cos(4 \cdot [\theta(r) - \theta(0)]) \quad (2.9)$$

Here, we provide the correlation functions in the $z=0$ plane for the 3D computational case using the parameters given in Table 2-1. For comparison, I also present results from 2D computational cases.

As for the pair correlation function (Figure 2-6 and Figure 2-7), both $g_{3D}(r)$ and $g_{2D}(r)$ from the 3D case have periodic peaks similar to $g_{2D}(r)$ (Figure 2-11), obtained using the 2D computational case. The difference is that in the 3D case the peak values are lower than for 2D. Therefore, one can conclude that some periodic structure exists in the 3D crystal, but that it is not as regular as in the 2D crystal. This type of $g_{3D}(r)$ has been observed in a recent experiment [Arp *et al.*, 2004].

As for the bond correlation functions, the value of the first peak in $G_4(r)$ is almost the same as in the 2D simulation case, which can support the conclusion that both the 2D and the 3D simulation results do not greatly exhibit the fourfold symmetry

properly. The six-fold bond correlation function $G_6(r)$ in the 3D case is smaller than in the 2D case, but much larger than the four-fold bond correlation function $G_4(r)$ in the 3D case. The results are not enough to conclude that the 3D lattice has a six-fold or a four-fold symmetry.

In order to verify the surface effect, we also analyzed the system's structure on the surface as shown in Figure 2-14, Figure 2-15, Figure 2-16, Figure 2-17 and Figure 2-18. The pictures were drawn by analyzing the x, y coordinates of the particles on the top surface. From Figure 2-15, which displays the particles' neighbor count, one can see that except for some defects on the surface, most of the particles on the surface have six neighbors, the same as in the 2D system. Therefore one can conclude that the surface has a regular lattice. However, the bond correlation functions on the surface (Figure 2-16, Figure 2-17 and Figure 2-18) do not show a large difference as compared to the $z=0$ plane that is located in the center of the simulation domain. A possible reason may be the curvature of the surface. Since the real surface is not a plane, the methods developed for the plane are not reliable for this surface.

We also performed a simulation case (Figure 2-19) with fewer particle numbers. In this case, the system displayed a multiple shell structure. In every layer, the lattice also had a regular symmetrical structure that should also be caused by the surface effect. As a result of small system size, surface effects can influence an entire system, causing multiple shell structures. The experimental analysis indicates that the particles also form a regular lattice in every shell [Arp *et al.*, 2004].

As for the surface effect itself, although the structure of the dusty plasma crystal in 2D or in the shell structure has been well studied, why larger systems do not show a regular lattice structure within the volume, but only on the surface is not well understood. The finite-size effect has been used to name the effect in the system with smaller size. Therefore, it does not seem very accurate to use in a large particle number system. Here, We call it a surface effect, and consider the surface effect and the finite-size effect as the same effect. I also provide some ideas regarding the nature of this effect. The first is the number of degrees of freedom. The surface effect leads to fewer degrees of freedom on the surface than for the general 3D system. With damping in the system, fewer degrees of freedom on the surface can make energy propagate further into the surface. As a result, small crystal pieces can align more particles beyond themselves. In addition to the degree of freedom, another factor is the magnitude of the confining force. The confining force in our simulation and in the experiments might not be strong enough, and may be responsible for break up the surface structure as we propagate into the volume.

Particles Position

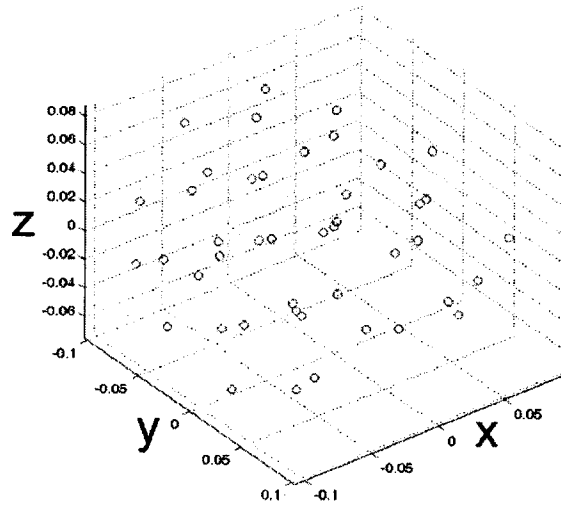


Figure 2-1: Particle positions in the 3D space

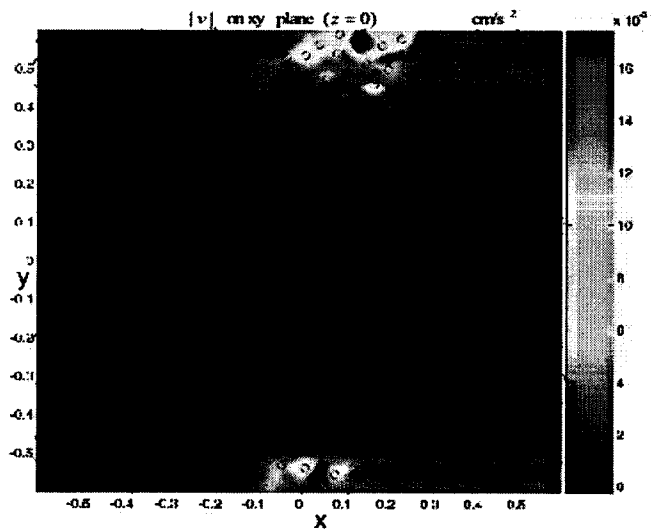


Figure 2-2: Particle position in X, Y coordinates in the $z=0$ cut plane; The color is the $|v|$

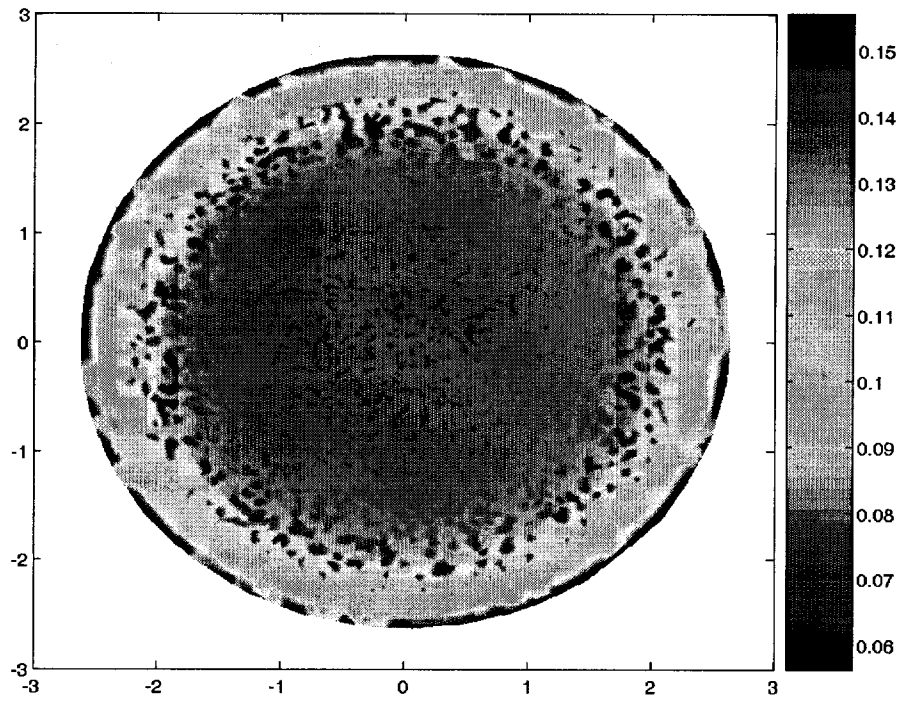


Figure 2-3: Particle separation of the whole crystal in the $z = 0$ plane;

The color is the particle separation, which is the same as following figures.

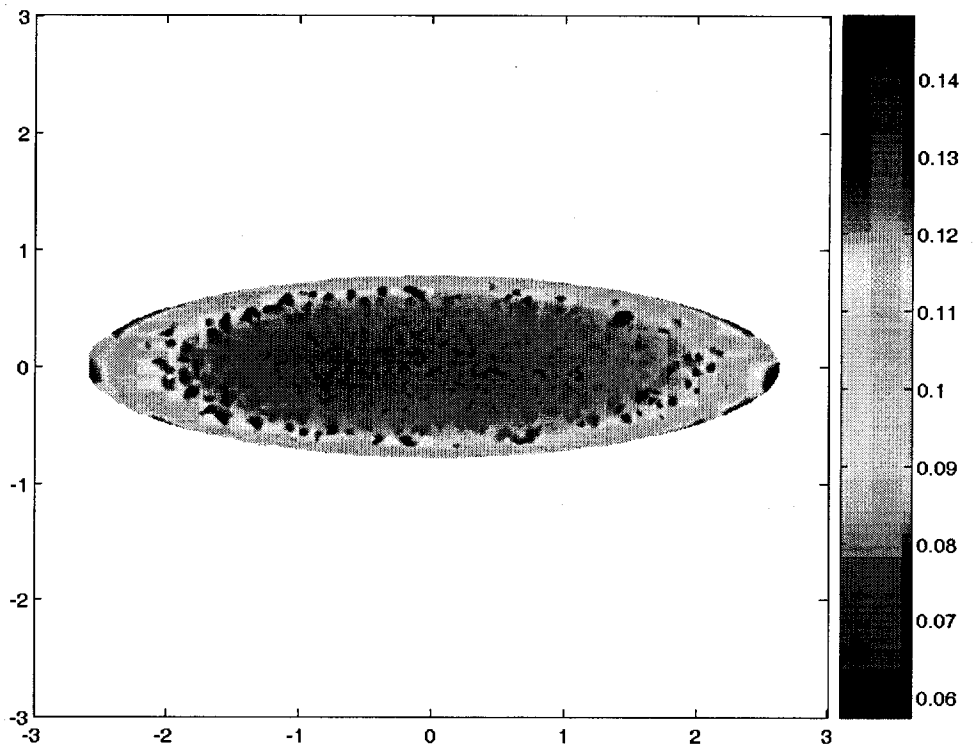


Figure 2-4: Particle separation of the whole crystal in the $x = 0$ plane

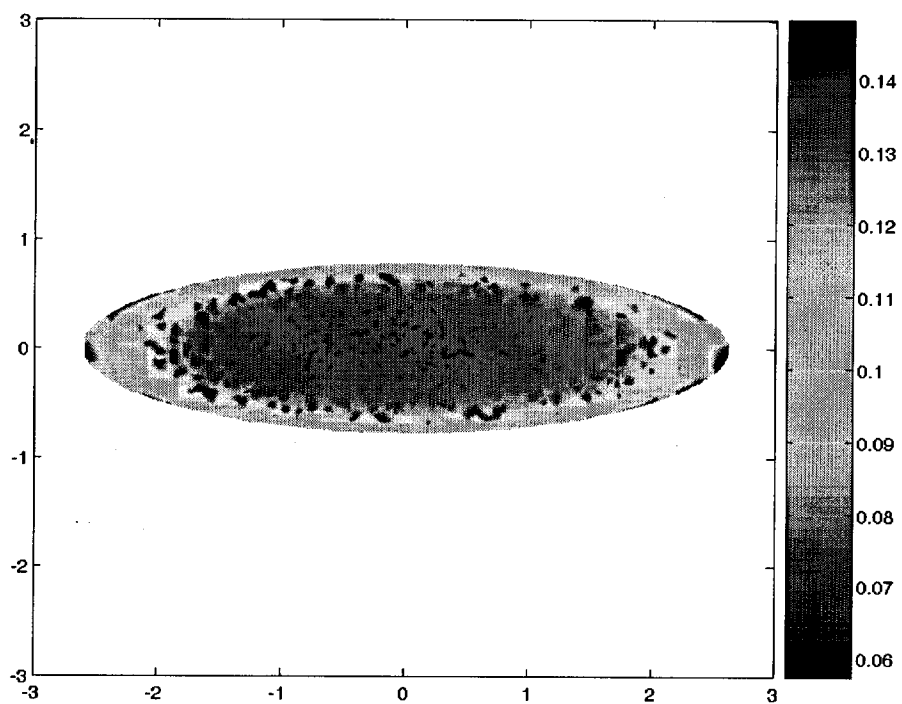


Figure 2-5: Particle separation of the whole crystal in the $y = 0$ plane

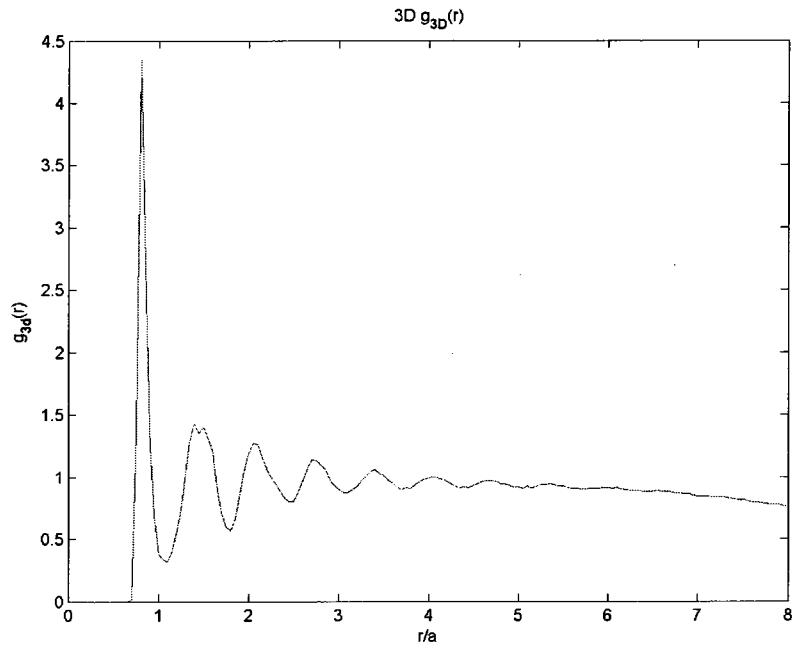


Figure 2-6: 3D $g_{3D}(r)$ for the whole crystal in the 3D computational case

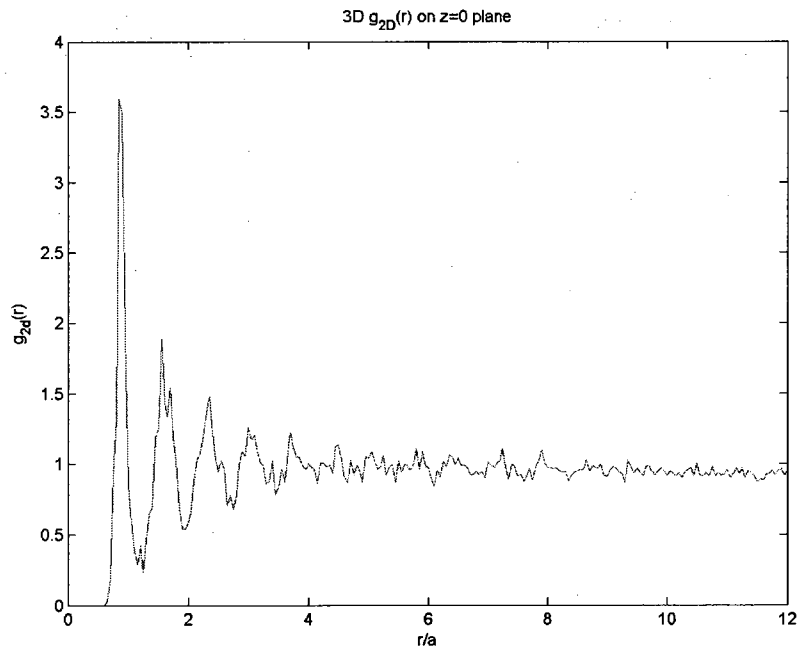


Figure 2-7: $g_{2D}(r)$ on the $z = 0$ plane in the 3D computational case

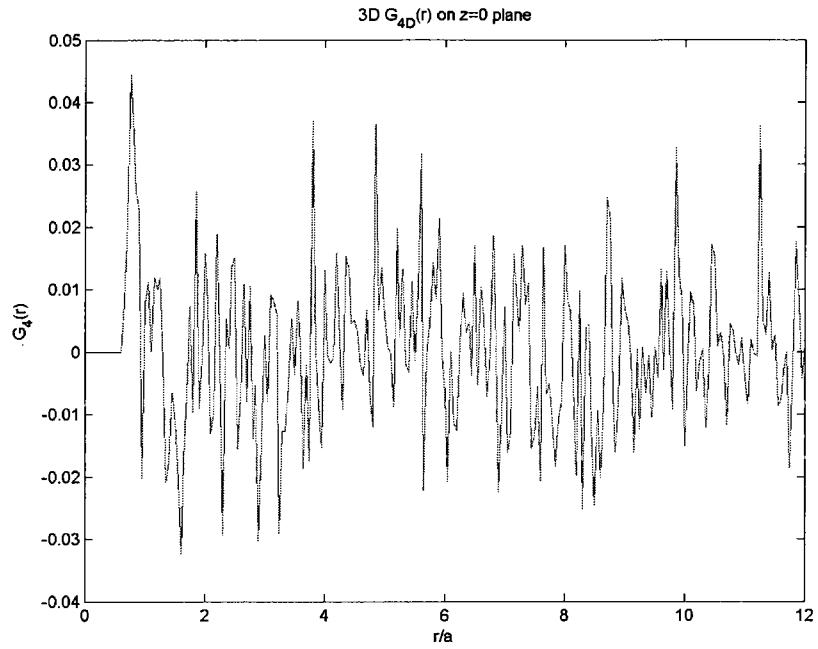


Figure 2-8: $G_4(r)$ on the $z = 0$ plane in the 3D computational case

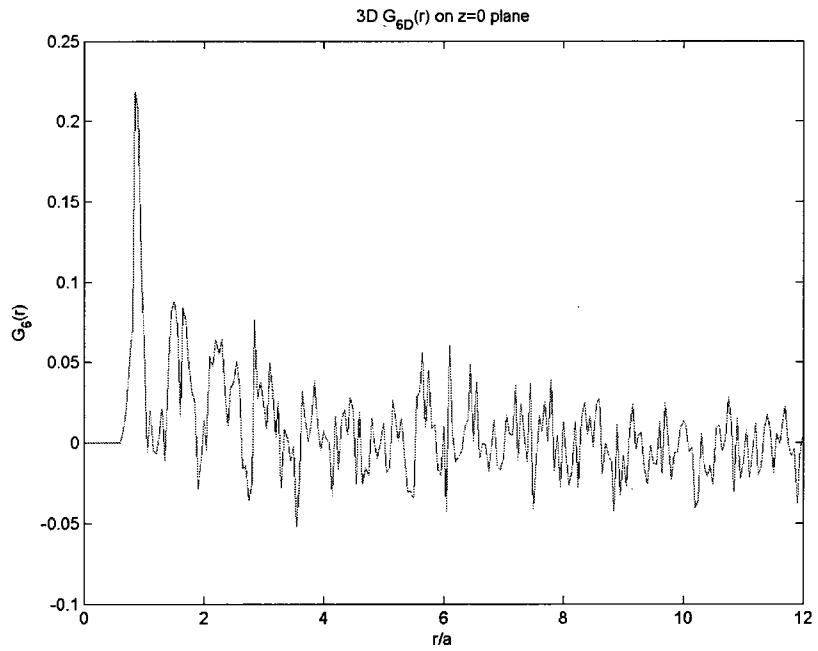


Figure 2-9: $G_6(r)$ on the $z = 0$ plane in the 3D computational case

2D result number of particle's neighbors

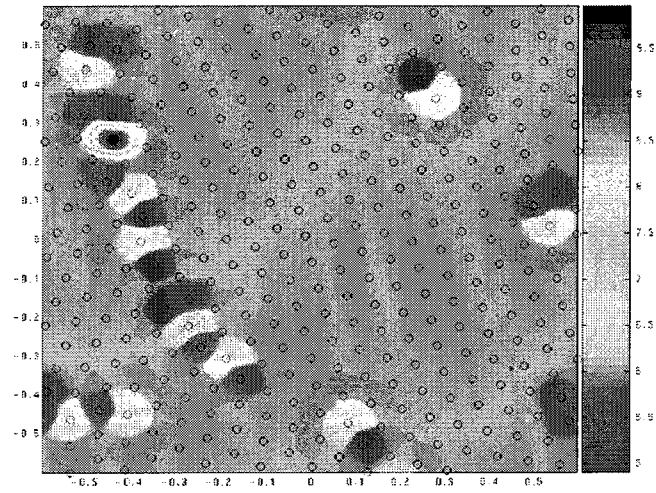


Figure 2-10: Count of the particles' neighbors in the 2D computational case

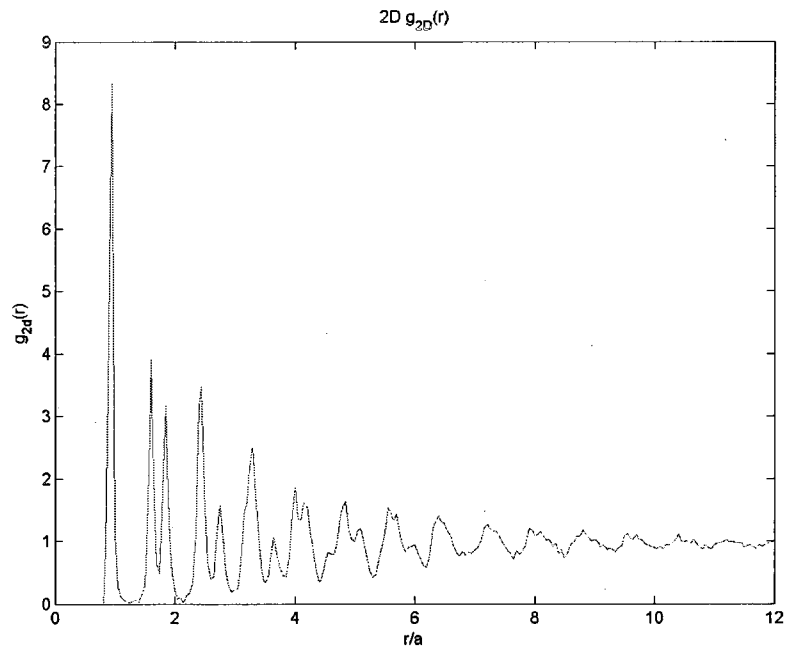


Figure 2-11: $g_{2D}(r)$ in the 2D computational case

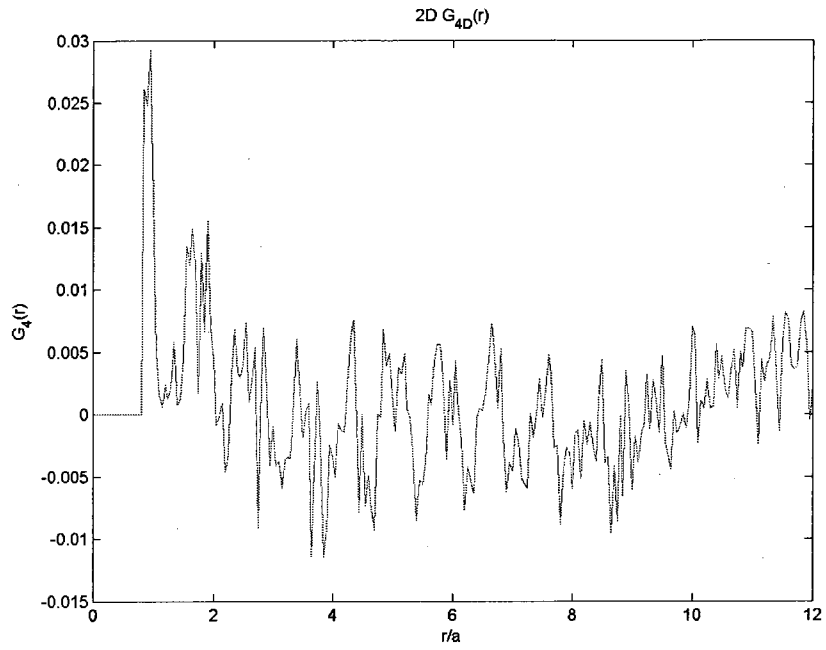


Figure 2-12: $G_4(r)$ in the 2D computational case

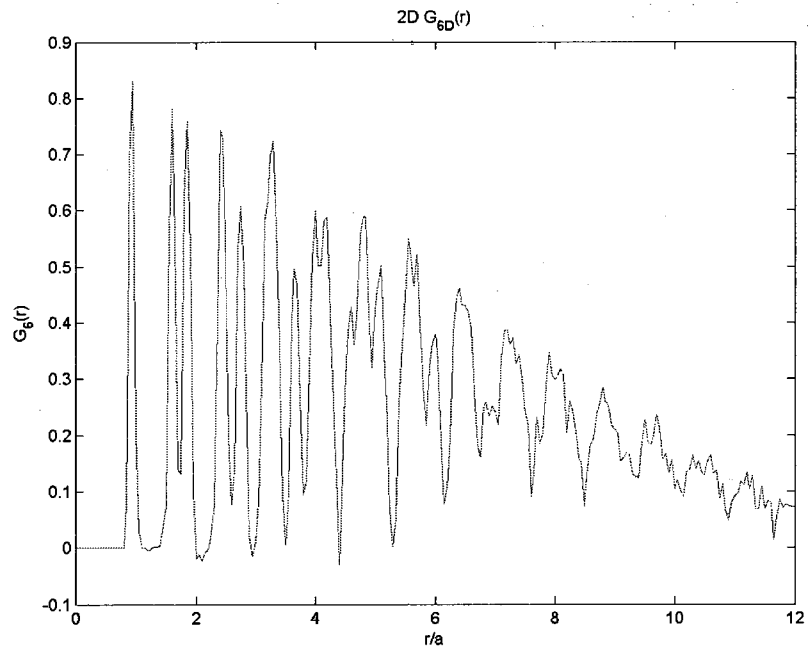


Figure 2-13: $G_6(r)$ in the 2D computational case

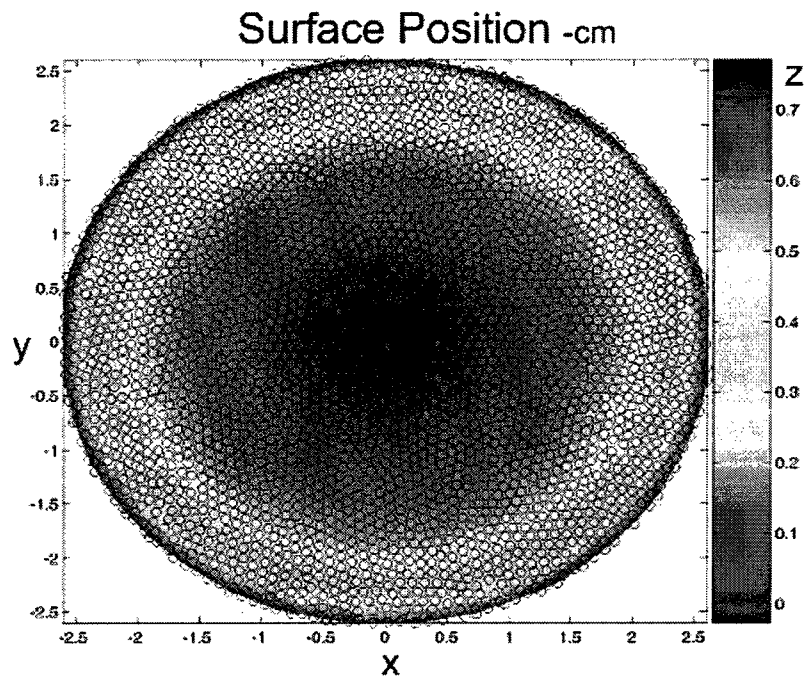


Figure 2-14: Particles' position on the top surface (The color is particle separation)

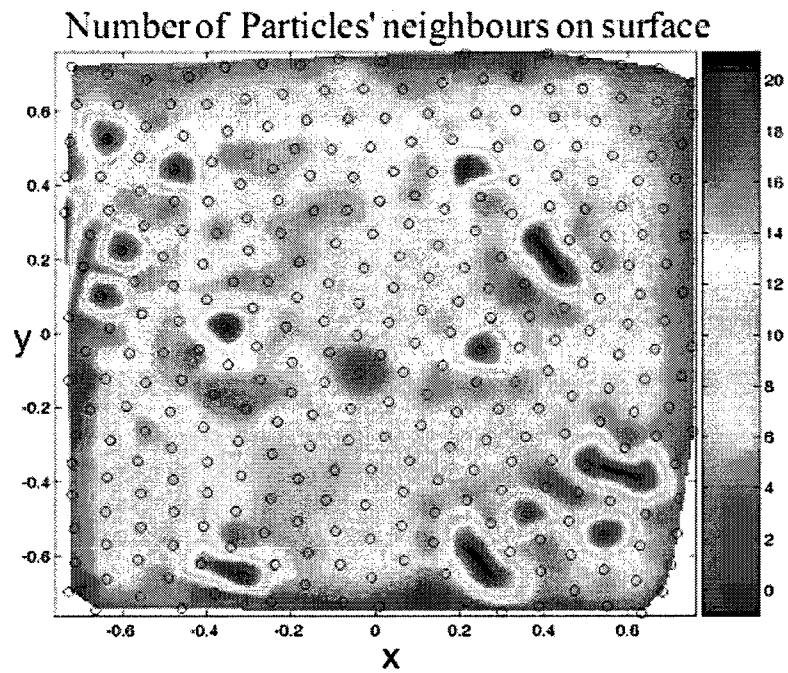


Figure 2-15: Count of particles' neighbors on the top surface

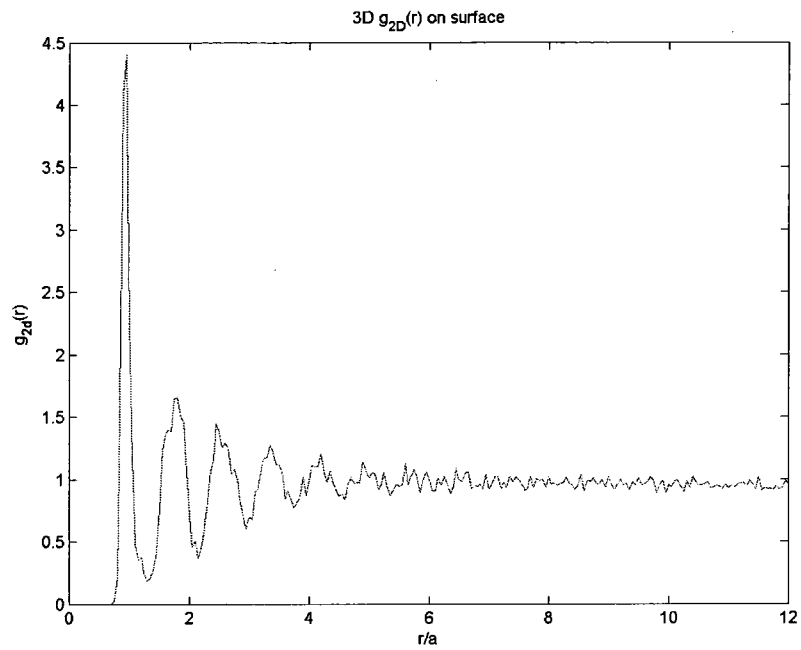


Figure 2-16: $g_{2D}(r)$ on the top surface according to particles' x, y positions

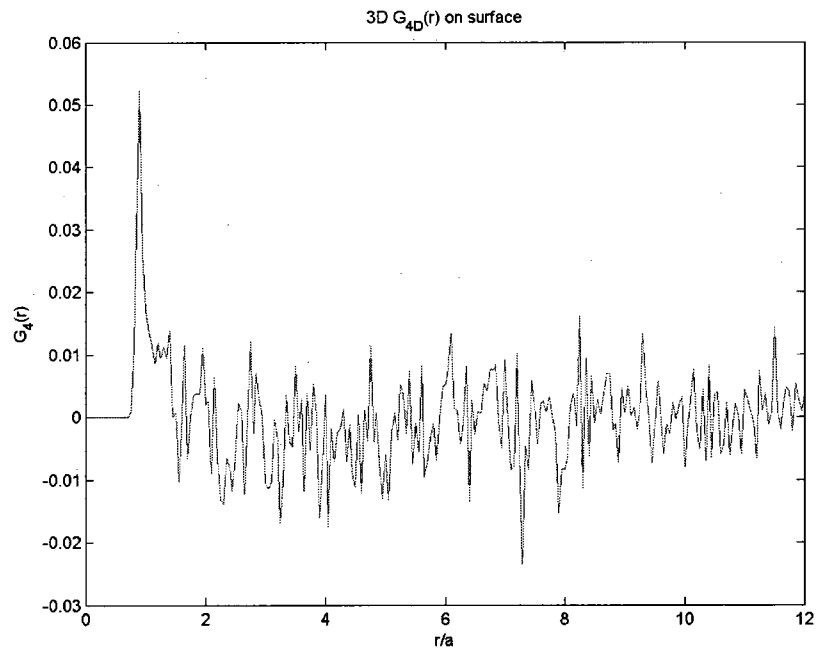


Figure 2-17: $G_4(r)$ on the top surface according to particles' x, y position

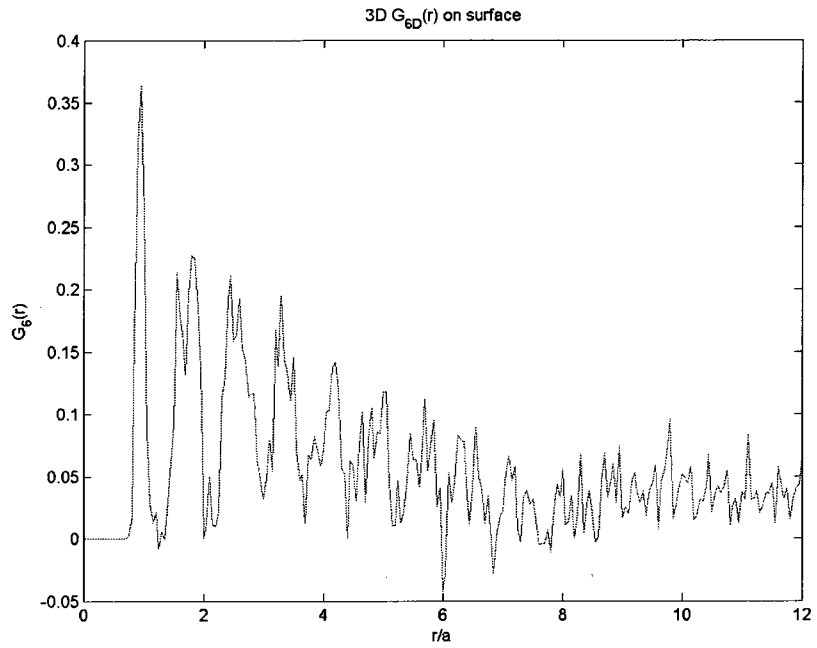


Figure 2-18: $G_6(r)$ on the top surface according to particles' x, y position

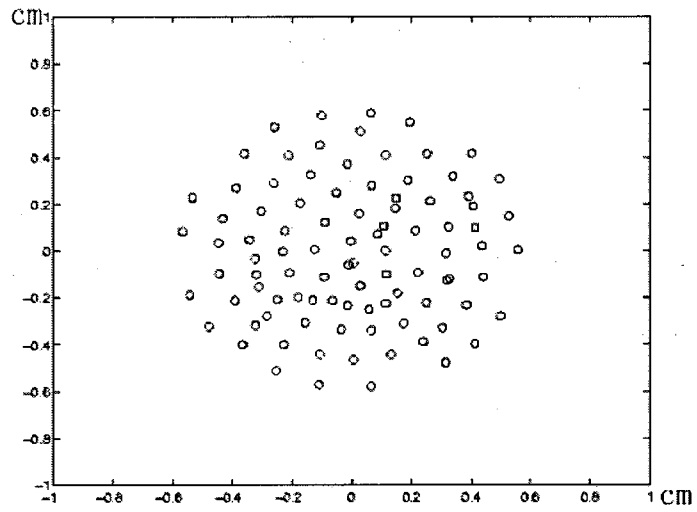


Figure 2-19: Particle's positions in $z = 0$ plane for 500-particle system

2.4 3D Mach Cone

In the perturbation stage of the simulation, laser forcing is added to the 3D dusty plasma crystal system that we obtained from the crystal forming stage of the simulation. The perturbation is used to simulate the effect of a laser in an experiment. Details of the 2D experiment and the corresponding simulation can be found in references [Ma and Bhattacharjee, 2002; Melzer et al., 2000; Samsonov et al., 1999].

The form of the laser perturbation in the simulation is obtained from Ma and Bhattacharjee's [2002] method, as shown in equation (2.3). Adding the laser perturbation to the center of a 3D dusty plasma system may be challenging in an experiment. In the simulation here, the perturbation amplitude is $f_0 = 5 \times 10^{-13} N$, and the spot moving speed is $V_L = 6.6$ cm/s. The force amplitude and the spot moving speed are larger than those utilized in the Ma's 2D simulation. The laser spot moved along the $y=0$ and the $z=0$ line.

The first character of the 3D Mach cone is that the Mach cone in 3D also displays a multiple Mach cone structure similar to the Mach cone in the 2D system. The 3D Mach cones have projections similar to those of 2D systems, as seen in Figure 2-20 through 2-28. Therefore, even though the crystal structure is different, the multiple Mach cone structure is qualitatively similar in the 2D and 3D dusty plasma crystal. Dubin and Wang et al. have analyzed eigenmodes in 2D dusty plasma crystals [Dubin, 2000; Xiaogang Wang, 2001]. From Dubin's work [Dubin, 2000], it is believed that the strong dispersive nature of the wave modes within the 2D system produces the multiple Mach cone

structure in 2D. So, waves in the 3D dusty plasma system should also have a very strong dispersive nature.

In 2D dusty plasma, it is difficult to distinguish Mach cones produced by shear waves vs. compressional waves. In 3D images, they are very easy to distinguish. For example, in our simulation, in the $z=0$, x,y plane, the v_x and v_y component contains both waves and has a larger speed than the shear wave. So, in Figure 2-23 and Figure 2-26 of v_x and v_y , the cone that is produced by compressional waves, has a larger size and can be easily identified. In 3D, on the $z=0$ plane, the v_z component is always perpendicular to the wave propagation direction. Therefore, Figure 2-28 for v_z only presents the result of the shearing wave, for which one can easily determine the shear wave cone. One can clearly find that the shear wave cone has a much smaller opening angle as compared to the cone produced by the compressional wave. Therefore, the shear wave should have a much smaller group wave speed than the shear wave. In 2D, since particle motion only has v_x and v_y components, it is difficult to observe the cone produced by the shear wave directly from these two components. In 2D, the perpendicular velocity v_z is always zero. Therefore, it is difficult to identify the shear wave cone in 2D pictures. An interesting property of the 3D system as compared to the 2D system is that the cone produced both by the compressional and the shear wave can be easily identified and separated.

The 3D Mach cone's size is also different than that in 2D. The Mach cones in 3D systems are smaller than the Mach cones in 2D systems, when both systems have similar

crystalline parameters and perturbation conditions. Figure 2-30 and Figure 2-27 are produced by the same perturbation amplitude, and drawn on the same scale. The crystal parameters are given in Table 2-1. The first reason for the size difference should lie within the respective volumes. If a perturbation of a given amplitude excites a given number of particles, then this number is almost the same as for both the 2D and the 3D systems. The 3D system can hold these particles within a smaller scale Mach cone than can the 2D system, where a larger scale size is needed. Therefore, the 3D Mach cone is smaller than the 2D Mach cone for the same plasma parameters and forcing conditions.

As described in the crystal analysis discussion, while the inner section of the 3D system does not have a regular lattice structure, the surface of the 3D system has a multiple-layer regular lattice structure. A perturbation is added on the surface (Figure 2-14) in order to produce a Mach cone. For this study, a laser spot moved along the surface. The properties of the Mach cone on the surface were found to be different from those of the Mach cone in the inner section of the system. A multiple Mach cone structure has not been previously observed on the surface of a 3D system. The simulation result with a V_L from 1.65 cm/s to 13.2 cm/s, is shown in Figure 2-31, Figure 2-32, Figure 2-33 and Figure 2-34. For a range of open angles, multiple Mach cones pattern is not observed. That the Mach cone on the surface is very different from the Mach cone in the central part of the system is expected since the dispersion relationship of the waves in the central section and in the surface region are different. The central section is composed of small pieces of lattice that make the central section almost isotropic. The surface region has multiple-layer structures that are anisotropic. Also previously observed is that open angles increase within deeper layers, Figure 2-35, and there is some evidence of multiple

Mach cone structure within these layers. I have also provided Mach cone pictures in the $y=0$ plane, as seen in Figure 2-42 and Figure 2-43. Using the surface perturbation above, one can observe that multiple cones can be produced in the center of the dusty plasma crystal. However, as we have seen for the surface, no multiple Mach cone can be determined in that layer.

One of the possible explanations for the fact that no multiple Mach cones are seen on the surface is that Mach cones are caused by the differences in the crystalline structures of the surface and inner sections. A difference in the crystalline structure could lead to different dispersive relationships of the waves on the surface, further more in the inner section that determines whether multiple Mach cones can exist.

Damping will also influence the size of the Mach cone, and can even make [Jiang *et al.*, 2009] the multiple Mach cone structure fade away, leaving only one Mach cone in the system. Our simulation also confirms this result. We tried to use the same perturbation parameter under different damping parameters, the ν in equation (2.1). As shown in Figure 2-36, Figure 2-37 and Figure 2-38 for the 2D system; and in Figure 2-39, Figure 2-40 and Figure 2-41 for the 3D system, when the damping force increases, the Mach cone structure fades away.

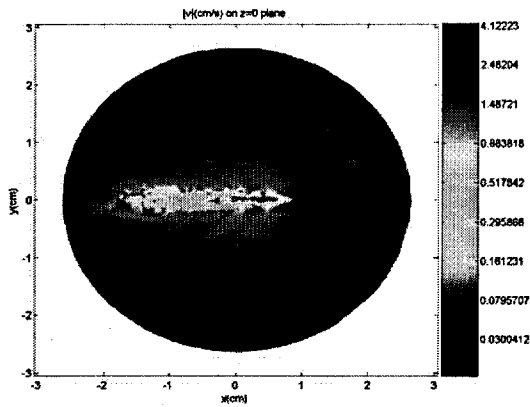


Figure 2-20: 3D Mach cone in the $(|v|)$ (cm) in the $z = 0$ plane)

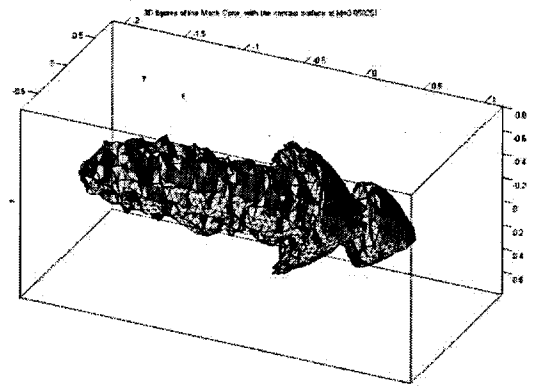


Figure 2-21: Mach cone in 3D system (3D figures)

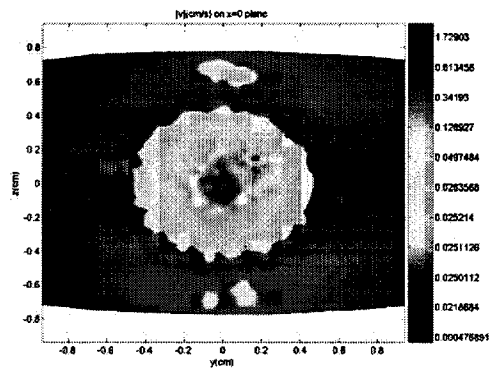


Figure 2-22: 3D Mach cone $(|v|)$ (cm) in the $x = 0$ plane)

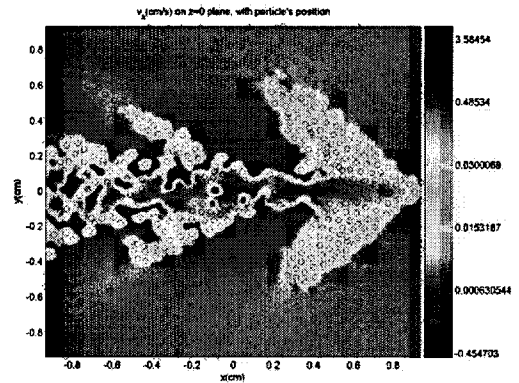


Figure 2-23: 3D Mach cone (v_x) in the $Z = 0$ plane)

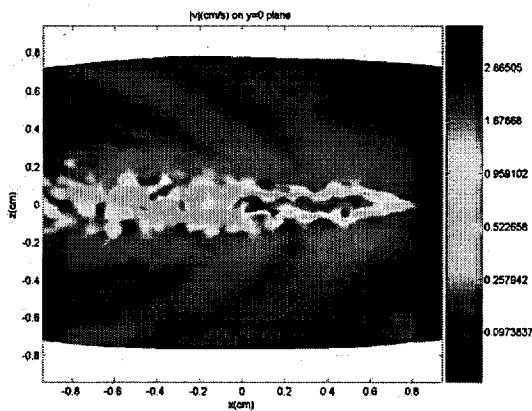


Figure 2-24: 3D Mach cone $(|v|)$ (cm) in the $y = 0$ plane)

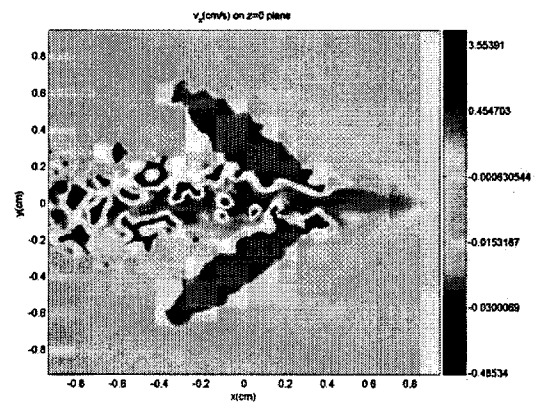


Figure 2-25: 3D Mach cone (v_x) in the $Z = 0$ plane), with apparent second wind

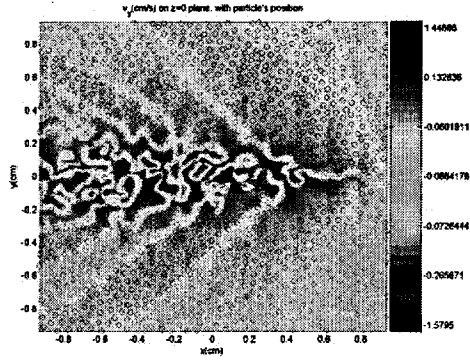


Figure 2-26: 3D Mach cone (v_y in the $z = 0$ plane)

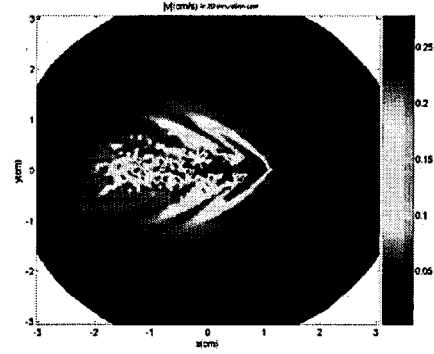


Figure 2-27: $|v|$ in 2D system, produced by $f_0 = 1.56 \times 10^{-13} \text{ N}$

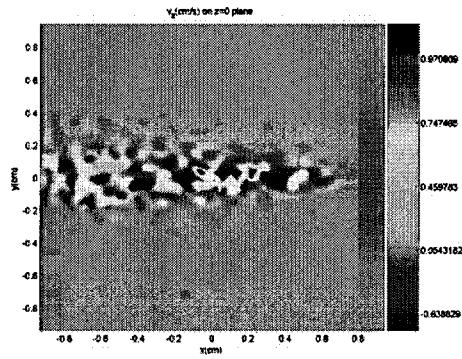


Figure 2-28: 3D Mach cone (v_z in the $z = 0$ plane)

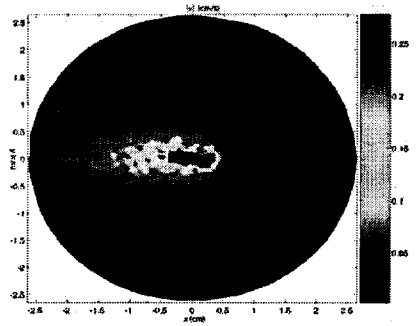


Figure 2-29: Mach cone on the surface produced by $f_0 = 1.56 \times 10^{-13} \text{ N}$ $V_L = 1.65 \text{ cm/s}$

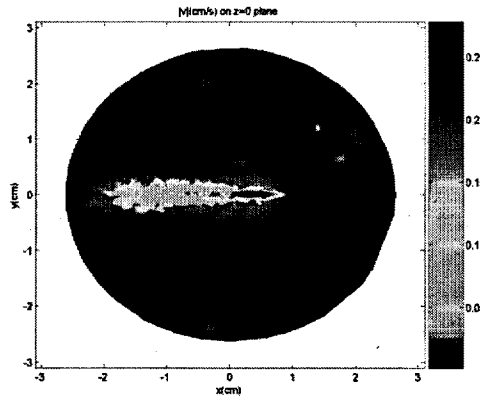


Figure 2-30: 3D Mach cone, $|v|$ in $z = 0$ plane, produced by $f_0 = 1.56 \times 10^{-13} \text{ N}$

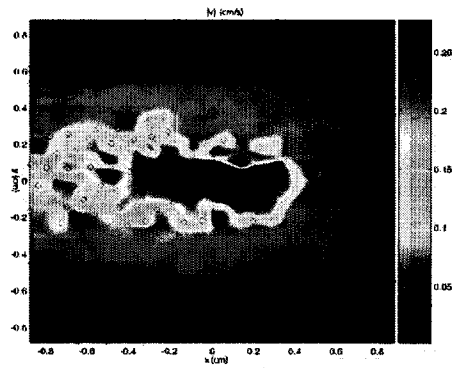


Figure 2-31: Mach cone on the surface produced by $f_0 = 1.56 \times 10^{-13} \text{ N}$ $V_L = 1.65 \text{ cm/s}$

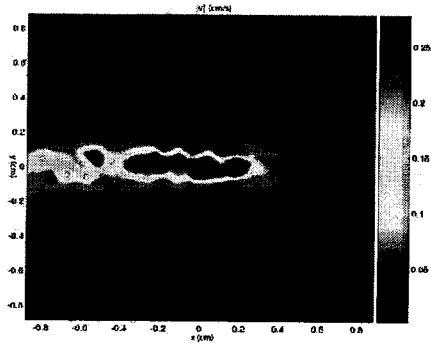


Figure 2-32: Mach cone on the surface produced by $f_0 = 1.56 \times 10^{-13} \text{ N}$, $V_L = 13.2 \text{ cm/s}$

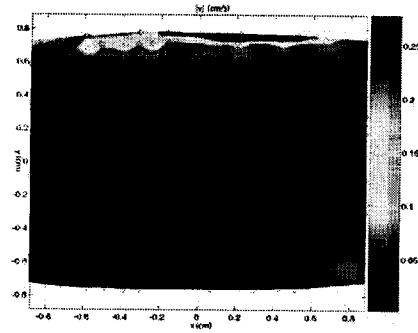


Figure 2-33: Side view of the Mach cone on the surface, produced by $f_0 = 9.9 \times 10^{-13} \text{ N}$, $V_L = 9.9 \text{ cm/s}$

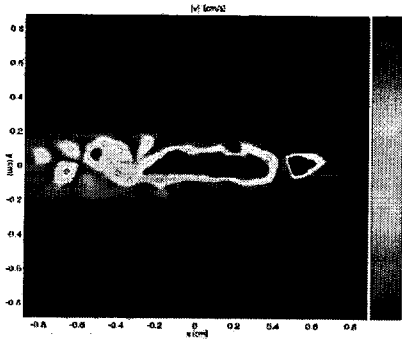


Figure 2-34: Mach cone on the surface produced by $f_0 = 9.9 \times 10^{-13} \text{ N}$, $V_L = 9.9 \text{ cm/s}$

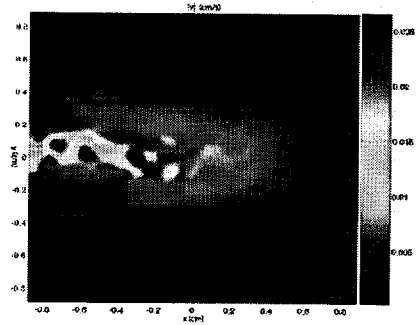


Figure 2-35: Mach cone on the $7a$ deep layer of the Yukawa crystal, produced by $f_0 = 9.9 \times 10^{-13} \text{ N}$, $V_L = 9.9 \text{ cm/s}$

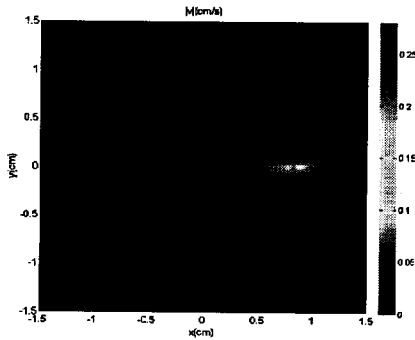


Figure 2-36: $|v|$ in the 2D system, produced by $f_0 = 1.56 \times 10^{-13} \text{ N}$ and $v = 270$

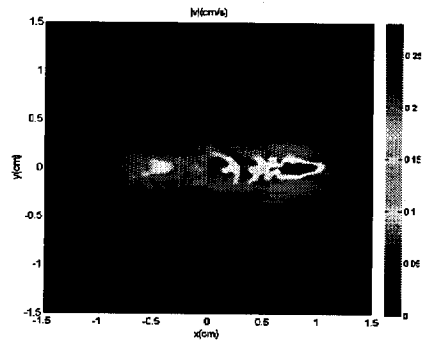


Figure 2-37: $|v|$ in the 2D system, produced by $f_0 = 1.56 \times 10^{-13} \text{ N}$ and $v = 27$

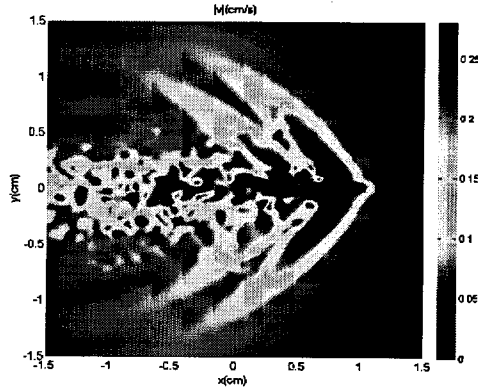


Figure 2-38: $|v|$ in the 2D system, produced by $f_0 = 1.56 \times 10^{-13} N$ and $\nu = 2.7$

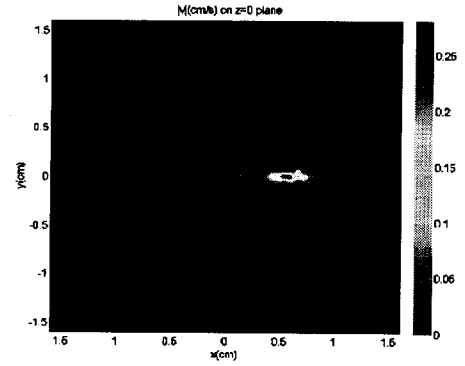


Figure 2-39: $|v|$ in the 3D system, produced by $f_0 = 5 \times 10^{-13} N$ and $\nu = 314$

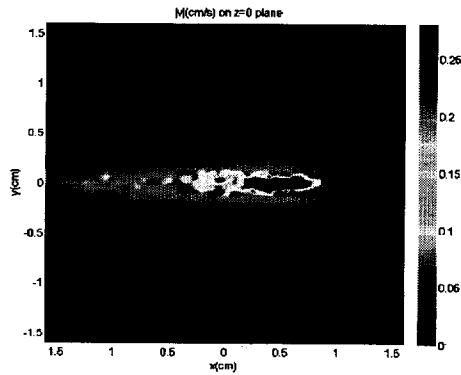


Figure 2-40: $|v|$ in the 3D system, produced by $f_0 = 5 \times 10^{-13} N$ and $\nu = 31.4$

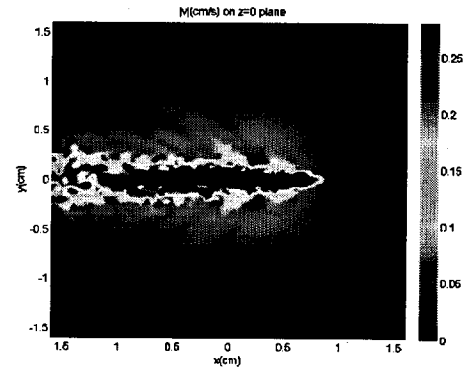


Figure 2-41: $|v|$ in the 3D system, produced by $f_0 = 5 \times 10^{-13} N$ and $\nu = 3.14$

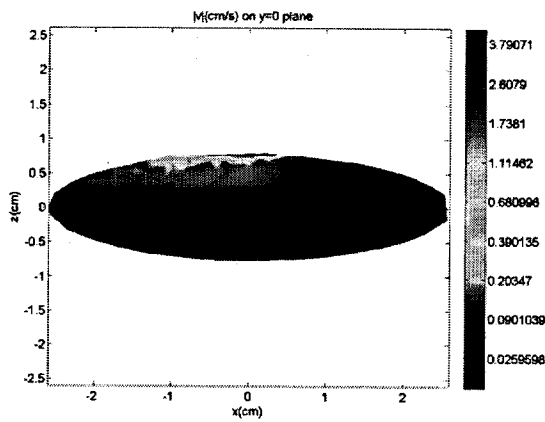


Figure 2-42: $|v|$ in the 3D system. The Mach cone is produced by perturbation on surface

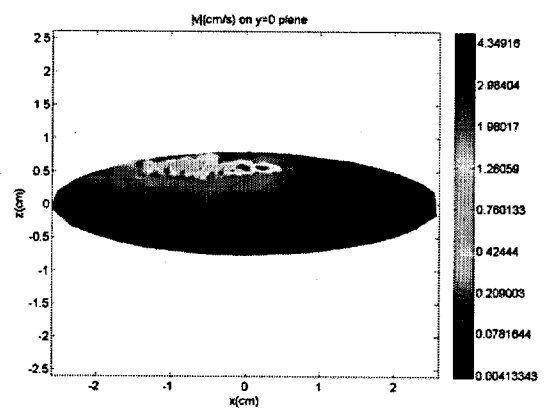


Figure 2-43: $|v|$ in the 3D system. The Mach cone is produced by perturbation under the surface

2.5 Conclusion

Chapter 2 presents the first simulation on 3D Mach cones in dusty plasma crystals. The particle number in our simulation is larger than other molecular simulations in the area of dusty plasma science. We found that the 3D Yukawa crystal and the 3D Mach cone in this system have the following properties:

- For systems with large particle numbers (more than 10,000), the central portion of the 3D crystal does not have as large a regular lattice as does the 2D crystal. On the surface of the 3D crystal, the lattice stills appears fairly regular. On the surface, a regular lattice can be observed.
- 3D multiple Mach cones can be achieved by adding certain perturbations to the 3D dusty plasma crystal. With similar crystal parameters, the same perturbation amplitude, and the same opening angles, the Mach cone size in 3D is smaller than in 2D.
- In the multiple-layer structure on the surface that exhibited regular lattices, no multiple Mach cone, as in the 2D system or in the 3D inner section, was observed.

Dubin [*Dubin, 2000*] has proposed that the physical mechanism that produces multiple Mach Cones in the 2D dusty plasma crystal are stable dispersive waves. Why the multiple Mach cone can still form in the inner part of the 3D system, and why the multiple Mach cone cannot be produced on the surface of the 3D system are still open questions. To answer these questions, one needs to develop theories of crystalline structure and wave modes in 3D dusty plasmas.

CHAPTER 3

APPLYING CENTPACK TO HALL MHD SIMULATIONS

In this chapter, I present Hall MHD simulations on the magnetic reconnection phenomenon. At first I introduce the numerical method and the details about applying KT central schemes in the Hall MHD simulation. Then I present numerical results from the dispersion relationship test and Hall MHD reconnection without electron inertia. Furthermore, I then present the Hall MHD simulation with electron inertia. A discussion regarding the numerical results is also provided at the end of this section.

3.1 Hall MHD Equation and Normalization

The successful implementation of non-oscillatory central schemes for the equations of ideal magnetohydrodynamics (MHD) and similar astrophysical models (see, for example, [*Jorge Balb'as and Tadmor, 2006a; Balbás et al., 2004; Del Zanna, 2003*]) and the versatility of this type of schemes, suggest their further development for computing the approximate solutions of other fluid models whose more complex characteristic decomposition makes the utilization of schemes based on Riemann solvers impractical. In this section, I present a high-resolution, non-oscillatory, central scheme for the Hall MHD model (3.1)-(3.7).

The numerical model discussed in this paper is based on the Hall magnetohydrodynamics (MHD) equations

$$\frac{\partial \rho}{\partial t} = -\nabla \cdot (\rho \mathbf{v}) \quad (3.1)$$

$$\frac{\partial \rho \mathbf{v}}{\partial t} = -\nabla \cdot \left\{ \rho \mathbf{v} \mathbf{v} + \bar{\mathbf{1}} \left(p + \frac{B^2}{2} \right) - \mathbf{B} \mathbf{B} \right\} \quad (3.2)$$

$$\frac{\partial U}{\partial t} = -\nabla \cdot \left\{ \left(U + p - \frac{B^2}{2} \right) \mathbf{v} + \mathbf{E} \times \mathbf{B} \right\} \quad (3.3)$$

$$\frac{\partial \mathbf{B}}{\partial t} = -\nabla \times \mathbf{E}. \quad (3.4)$$

Within the above equations, the following terms are

$$\mathbf{j} = \nabla \times \mathbf{B} \quad (3.5)$$

$$U = \frac{p}{\gamma - 1} + \frac{\rho v^2}{2} + \frac{B^2}{2} \quad (3.6)$$

$$\mathbf{E} = -\mathbf{v} \times \mathbf{B} + \eta \mathbf{j} + \frac{\mathbf{j} \times \mathbf{B}}{e(\rho / m_i)} + \frac{m_e}{e^2(\rho / m_i)} \left[\frac{\partial \mathbf{j}}{\partial t} + (\mathbf{v} \cdot \nabla) \mathbf{j} \right]. \quad (3.7)$$

Equation (3.7) is the so called generalized Ohm's law. Equations (3.1), (3.2) and (3.3) are the mass conservation, momentum conservation and energy conservations. Equation (3.4) is not a conservation law. Instead it is the Faraday's law of induction. It is Faraday's induction that makes the MHD system hyperbolic.

Normalizing the above equation in the same manner as was adopted for the Geospace Environment Modeling (GEM) challenge [Birn *et al.*, 2001], we get:

$$L_0 = \delta_i = \frac{v_A}{\omega_{ci}} = \frac{m_i}{e\sqrt{\mu_0 \rho_0}} = \frac{c}{\omega_{pi}} = \frac{1}{e} \sqrt{\frac{m_i}{n_0 \mu_0}} \quad (3.8)$$

$$\delta_e = \frac{v_A}{\omega_{ce}} = \frac{m_e}{e\sqrt{\mu_0 \rho_0}} = \frac{c}{\omega_{pe}} = \frac{1}{e} \sqrt{\frac{m_e}{n_0 \mu_0}} \quad (3.9)$$

$$t_0 = \frac{1}{\omega_{ci}} = \frac{m_i}{eB_0} \quad (3.10)$$

$$v_0 = v_A = \frac{B_0}{\sqrt{\mu_0 \rho_0}} = \frac{L_0}{t_0} \quad (3.11)$$

$$p_0 = \beta_0 \frac{B_0^2}{2\mu_0} \quad \text{and usually } \beta_0 = 2 \quad (3.12)$$

$$T_0 = \frac{p_0}{n_0 k} = \frac{B_0^2}{2\mu_0 n_0 k} \quad (3.13)$$

$$E_0 = v_0 B_0 = \frac{B_0^2}{\sqrt{\mu_0 \rho_0}} \quad (3.14)$$

$$j_0 = \frac{B_0}{\mu_0 L_0} = \frac{B_0 e \sqrt{n_0}}{\sqrt{\mu_0 m_i}} \quad (3.15)$$

Then, equations (3.1)-(3.7) can be written as (3.16)-(3.22), and all of the terms become dimensionless.

$$\frac{\partial \rho}{\partial t} = -\nabla \cdot (\rho \mathbf{v}) \quad (3.16)$$

$$\frac{\partial \rho \mathbf{v}}{\partial t} = -\nabla \cdot \left\{ \rho \mathbf{v} \mathbf{v} + \bar{\mathbf{1}} \left(p + \frac{B^2}{2} \right) - \mathbf{B} \mathbf{B} \right\} \quad (3.17)$$

$$\frac{\partial U}{\partial t} = -\nabla \cdot \left\{ \left(U + p - \frac{B^2}{2} \right) \mathbf{v} + \mathbf{E} \times \mathbf{B} \right\} \quad (3.18)$$

$$\frac{\partial \mathbf{B}}{\partial t} = -\nabla \times \mathbf{E} \quad (3.19)$$

$$\mathbf{j} = \nabla \times \mathbf{B} \quad (3.20)$$

$$U = \frac{p}{\gamma-1} + \frac{\rho v^2}{2} + \frac{B^2}{2} \quad (3.21)$$

$$\mathbf{E} = -\mathbf{v} \times \mathbf{B} + \eta \mathbf{j} + \frac{\mathbf{j} \times \mathbf{B}}{\rho} + \frac{m_e}{m_i} \frac{1}{\rho} \left[\frac{\partial \mathbf{j}}{\partial t} + (\mathbf{v} \cdot \nabla) \mathbf{j} \right] \quad (3.22)$$

$$\left(\frac{\delta_e}{L_0} \right)^2 = \left(\frac{\delta_e}{\delta_i} \right)^2 = \frac{m_e}{m_i} \quad (3.23).$$

In above equations, the ion inertial length, δ_i , is the length that an electromagnetic wave can propagate in time $1/\omega_{pi}$. The term ω_{pi} is the ion plasma oscillation frequency. The ion inertial length, δ_i , could also be the length that an Alfvén wave propagates in a time of $1/\omega_{ci}$. The term ω_{ci} is the cyclotron frequency, and v_A is the Alfvén wave speed. In the simulations presented in this thesis, we have chosen $L_0 = \delta_i$.

We will use the Hall MHD model to study the magnetic reconnection with different length scale assumptions. For most cases, the shortest length scale is the current sheet width. For equation (3.22), if the current sheet width is much larger than δ_i , the terms after the resistivity can all be ignored. When the current sheet width approaches δ_i , but still much larger than δ_e , the third and fourth term on the right hand side of the equation cannot be ignored. The third term is the so-call Hall MHD term. When this $\mathbf{J} \times \mathbf{B}$ term is added into the MHD equation, we call the MHD equations as the Hall MHD equations. A more complete generalized Ohm's law includes the pressure tensor term, which is hard to treat in a fluid system because of the lack of closure equations for the various elements of the pressure tensor in terms of fluid variables. The PIC simulations shows that the pressure is playing a major term in the diffusive region in the

generalized Ohm's law. But the role of this term is still an open question. In what follows we have neglected the effects of the pressure tensor. When the current sheet width is no longer much larger than δ_e , the last term can no longer be ignored. This last term is the electron inertia term. If the mass of the electron is zero this term will no longer exist. The zero mass assumption is the basic assumption in the resistive Hall MHD simulation. In practical terms, as long as the resistive width of the thin current sheet produced during reconnection dynamics remains larger than the electron skin depth, it is valid to ignore the electron inertia term.

The role of the Hall MHD term and the electron inertia term in magnetic reconnection is still a matter of debate. The linear analysis will tell us how the dispersion relationship of the MHD system will be changed after the MHD term and the electron inertia term are added.

Details of a classical linear analysis of the MHD equation can be found in textbooks [*Gurnett and Bhattacharjee, 2005*], which tells us that the speed of the Alfvén wave in the MHD system is not related to the wave length. We performed a similar analysis on the Hall MHD equations (3.16)-(3.22). For transverse waves that travel in the same direction as the magnetic field, we can obtain a dispersion relationship for Hall MHD ($\delta_e = 0$), as follows:

$$\frac{\omega}{k} = \frac{B_0}{\sqrt{\rho_0}} \frac{k + \sqrt{k^2 + 4}}{2} \quad (3.24)$$

$$\frac{d\omega}{dk} = \frac{B_0}{\sqrt{\rho_0}} \left(k + \frac{k^2 + 2}{\sqrt{k^2 + 4}} \right) \quad (3.25)$$

For $\delta_e > 0$, a linear analysis could tell us, while ignoring the $(\mathbf{v} \cdot \nabla)\mathbf{j}$ term:

$$\frac{\omega}{k} = \frac{B_0}{\sqrt{\rho_0}} \frac{k + \sqrt{k^2 + 4(1 + \delta_e^2 k^2)}}{2(1 + \delta_e^2 k^2)} \quad (3.26)$$

When deriving the above dispersive relationship, we assume the perturbation is only in x direction, which is the same direction as the unperturbed background magnetic field. The perturbation of the magnetic field and the velocity only have y, z component, which are perpendicular to the wave propagating direction. The numerical test in section 3.3 is designed to satisfy the assumptions here.

Diagrams of the two dispersion relationships can be found in Figure 3-1 as green lines. For the Hall MHD, one finds that when the wave number, k , becomes larger, the phase velocity, which is the slope of the green line in the upper right-hand figure of Figure 4-1, also increases. Phase velocity is the wave profile traveling speed. As for group velocity, the actual travel speed for information and energy, it increases even faster than the phase velocity. In the numerical simulation, researchers often use the phase velocity when discussing the CFL condition, which can be problematic.

When electron inertia is included, one finds that when the wave number, k , increases to a certain level, at a scale of $1/\delta_e$, the phase velocity no longer increases. When the wave number, k , increases to an even large number, the phase velocity begins to decrease. But at this scale, these waves might not be the dominant wave.

3.2 Applying Kurganov and Tadmor Central Schemes in Hall MHD

3.2.1 Central Schemes

In this section I will introduce how the Kurganov and Tadmor Central schemes were applied in the Hall MHD simulation, and discuss the difficulty researchers face in Hall MHD reconnection simulations. Usually the numerical schemes for hyperbolic equations can be divided into central schemes and upwind schemes. For upwind-type differencing schemes, the hyperbolic partial differential equations is discretized based on the direction of the information or energy flowing direction. In central schemes, the discretization will not be related to the flow [Culbert B. Laney (1998)].

Both Hall and the electron inertia terms in equation (3.22) pose significant numerical challenges for simulating MHD flows. Unlike in classical MHD where the characteristic speeds remain constant with respect to the wave frequency, the whistler wave in Hall MHD satisfies the dispersion relation $v \sim k$ (where k is related to the wave frequency by $\omega \sim k^2$ [D. Biskamp, 1997], and v is the phase velocity). Thus, the Alfvén wave speed increases when the wave length becomes small, $v \sim 1/\Delta x$, and the maximum wave speed increases as the grid is refined, $v_{max} \sim 1/\Delta x$, requiring extremely small time steps that may take too long to complete and result in too much numerical dissipation.

Results previously obtained using central schemes for ideal MHD flows [Jorge Balb'as and Tadmor, 2006a; J. Balb'as et al., 2004], and the minimal characteristic information from the underlying PDE they required, suggest the central schemes as the building block for new schemes to solve more complex MHD flows. In particular, we turn our attention to the semi-discrete central formulation of Kurganov and Tadmor (KT)

schemes [Kurganova and Tadmor, 2000] that have a numerical viscosity as $\mathcal{O}((\Delta x)^{2r-1})$, in which r is the numerical accuracy order of the schemes. Most fully-discrete central schemes, such as the Nessyahu-Tadmor (NT) schemes, have the numerical viscosity of order $\mathcal{O}((\Delta x)^{2r}/\Delta t)$. The numerical viscosity of the fully discrete central schemes will increase sharply when time step, Δt , becomes small. The advantage of using KT schemes is that the numerical viscosity will not increase when the time steps become small, and that they allow larger time steps than the fully-discrete schemes. The small viscosity makes semi-discrete central schemes produce very stable numerical results, with no worse accuracy than for other explicitly numerical schemes. The software package CentPACK, that implements KT schemes, can decouple the numerical schemes and the physics that it simulates, so researchers can focus on the physics rather than on programming.

Here we are going through the process of constructing the central schemes we are using following reference [Jorge Balb'as and Tadmor, 2006a]. We begin by re-writing the equations (3.16)-(3.19) in the conservation form, as follows:

$$u_t + f(u)_x + g(u)_y = 0 \quad (3.27)$$

$$u = (\rho, \rho v_x, \rho v_y, \rho v_z, B_x, B_y, B_z, U)^T \quad (3.28)$$

$$f(u) = (\rho v_x, \rho v_x v_x + p + \frac{B^2}{2} - B_x^2, \rho v_x v_y - B_x B_y, \rho v_x v_z - B_x B_z, 0, -E_z, E_y, (U + p - \frac{B^2}{2})v_x + E_y B_z - E_z B_y)^T \quad (3.29)$$

$$g(u) = (\rho v_y, \rho v_x v_y - B_y B_x, \rho v_y v_y + p + \frac{B^2}{2} - B_y^2, \rho v_y v_z - B_y B_z, E_z, 0, -E_x(U + p - \frac{B^2}{2})v_x + E_z B_x - E_x B_z)^T, \quad (3.30)$$

The electric fields are given by:

$$\begin{pmatrix} E_x \\ E_y \\ E_z \end{pmatrix} = -\mathbf{v} \times \mathbf{B} + \eta \begin{pmatrix} j_x \\ j_y \\ j_z \end{pmatrix} + \eta_j \begin{pmatrix} \nabla^2 j_x \\ \nabla^2 j_y \\ \nabla^2 j_z \end{pmatrix} + \frac{\mathbf{j} \times \mathbf{B}}{\rho} + \frac{m_e}{m_i} \frac{1}{\rho} \left\{ \frac{\partial}{\partial t} + (v_x \frac{\partial}{\partial x} + v_y \frac{\partial}{\partial y} + v_z \frac{\partial}{\partial z}) \right\} \begin{pmatrix} j_x \\ j_y \\ j_z \end{pmatrix} \quad (3.31)$$

$$\begin{pmatrix} j_x \\ j_y \\ j_z \end{pmatrix} = \begin{pmatrix} \frac{\partial B_z}{\partial y} \\ -\frac{\partial B_z}{\partial x} \\ \frac{\partial B_y}{\partial x} \end{pmatrix} \quad (3.32)$$

Central schemes realize the solution of the hyperbolic conservation law in terms of the cell average of u over the control volume $I_{i,j} = [x_{i-1/2}, x_{i+1/2}] \times [y_{j-1/2}, y_{j+1/2}]$,

$$\bar{u}_{i,j}(t) = \frac{1}{\Delta x \Delta y} \int_{x_i - \frac{\Delta x}{2}}^{x_i + \frac{\Delta x}{2}} \int_{y_j - \frac{\Delta y}{2}}^{y_j + \frac{\Delta y}{2}} u(x, y, t) dy dx. \quad (3.33)$$

Integrating (3.33) over $I_{i,j}$ and dividing by the space scales Δx and Δy , yields the equivalent formulation, as follows:

$$\begin{aligned} \frac{d\bar{u}_{i,j}(t)}{dt} = & -\frac{1}{\Delta x \Delta y} \left[\int_{y_{j-1/2}}^{y_{j+1/2}} \left(f(u(x_{i+1/2}, y)) - f(u(x_{i-1/2}, y)) \right) dy \right. \\ & \left. + \int_{x_{i-1/2}}^{x_{i+1/2}} \left(g(u(x, y_{j+1/2})) - g(u(x, y_{j-1/2})) \right) dx \right], \end{aligned} \quad (3.34)$$

which can be re-written in the more compact form

$$\frac{d\bar{u}_j(t)}{dt} = -\frac{1}{\Delta x} \left[H^x_{i+\frac{1}{2},j} - H^x_{i-\frac{1}{2},j} \right] - \frac{1}{\Delta y} \left[H^y_{i,j+\frac{1}{2}} - H^y_{i,j-\frac{1}{2}} \right], \quad (3.35)$$

where the numerical fluxes $H^x_{i\pm\frac{1}{2},j}$ and $H^y_{i,j\pm\frac{1}{2}}$ approximate the integrals on the right of (3.34) and are calculated to account for the propagation of the discontinuities at the cell interfaces $x = x_{i\pm\frac{1}{2}}$ and $y = y_{j\pm\frac{1}{2}}$.

For the results presented below, we chose the midpoint rule for approximating the integrals that result in the fluxes, as follows:

$$\begin{aligned} H^x_{i+\frac{1}{2},j} &= \frac{f(u_{i+1,j}^W) + f(u_{i,j}^E)}{2} - \frac{\alpha^x_{i+\frac{1}{2},j}}{2} (u_{i+1,j}^W - u_{i,j}^E) \\ H^y_{i,j+\frac{1}{2}} &= \frac{g(u_{i,j+1}^S) + g(u_{i,j}^N)}{2} - \frac{\alpha^y_{i,j+\frac{1}{2}}}{2} (u_{i,j+1}^S - u_{i,j}^N). \end{aligned} \quad (3.36)$$

For the actual implementation of the scheme, the values of $u(x, y, t)$ at the cell interfaces $u_{i,j}^{N/S,E/W}(t)$ are recovered via a non-oscillatory, piece-wise polynomial reconstruction

$R(x, y; \bar{u}(t)) = \sum_{i,j} p_{i,j}(x, y) \cdot \mathbf{1}_{I_{i,j}}(x, y)$, and defined as

$$\begin{aligned} u_{i,j}^E &:= p_{i,j}(x_{i+\frac{1}{2}}, y_j) & u_{i,j}^W &:= p_{i,j}(x_{i-\frac{1}{2}}, y_j) \\ u_{i,j}^N &:= p_{i,j}(x_i, y_{j+\frac{1}{2}}) & u_{i,j}^S &:= p_{i,j}(x_i, y_{j-\frac{1}{2}}), \end{aligned} \quad (3.37)$$

where $\alpha^x_{i+\frac{1}{2}}$ and $\alpha^y_{i,j+\frac{1}{2}}$ stand for the maximum speeds of propagation at the cell interfaces in the x and y directions respectively; we approximate these by

$$\alpha^x_{i+\frac{1}{2}} = \max \left\{ \rho(u_{i+1,j}^W), \rho(u_{i,j}^E) \right\}, \quad \alpha^y_{i,j+\frac{1}{2}} = \max \left\{ \sigma(u_{i,j+1}^S), \sigma(u_{i,j}^N) \right\}, \quad (3.38)$$

where ρ and σ stand for the spectral radius of the Jacobian matrices of $f(u)$ and $g(u)$

respectively. These values will, indeed, be exact if $f(u)$ and $g(u)$ are convex. For the second order scheme that we propose, the interface values are reconstructed from the cell averages via the bi-linear functions

$$p_{i,j}(x,y) = \bar{u}_{i,j} + (u_x)_{i,j}(x-x_i) + (u_y)_{i,j}(y-y_j) \quad (3.39)$$

with the numerical derivatives of u on x direction $(u_x)_{i,j}$ approximated with the limiter, [van Leer, 1979],

$$(u_x)_{i,j} = \min \text{mod } 3 \left\{ \frac{\bar{u}_{i+1,j} - \bar{u}_{i,j}}{\Delta x}, \frac{\bar{u}_{i+1,j} - \bar{u}_{i-1,j}}{2\Delta x}, \frac{\bar{u}_{i,j} - \bar{u}_{i-1,j}}{\Delta x} \right\}, \quad (3.40)$$

and similarly for $(u_y)_{i,j}$, where:

$$\begin{aligned} \min \text{mod } \{a, b\} &= (\text{sgn}(a) + \text{sgn}(b)) \min \{|a|, |b|\} \\ \min \text{mod } 3 \{a, b, c\} &= \min \text{mod } \{ \min \text{mod } \{a, b\}, \min \text{mod } \{b, c\} \} \end{aligned} \quad (3.41)$$

The minmod based reconstruction is an Essentially Non-Oscillatory (ENO) reconstruction and satisfies the total-variation diminishing (TVD) [Culbert B. Laney (1998)], hence the corresponding central schemes are TVD and ENO. The higher order non-oscillatory extension of the second reconstruction algorithms are offered by the ENO reconstruction of Harten etc. [Harten et al., 1987] and their implementation with central schemes can be found in this reference [Levy et al., 2002].

Once the point values in equation (3.37) are recovered and the speeds of propagation in equation (3.38) estimated so as to compute the numerical fluxes in equation (3.36), an evolution routine can be employed to evolve the cell averages of u . We choose a second order SSP Runge-Kutta scheme, [Gottlieb et al., 2001], for the simulations below,

$$\begin{aligned}
u^{(1)} &= u^n + \Delta t C(u^n), \\
u^{n+1} &= u^{(1)} + \frac{\Delta t}{2} [C(u^{(1)}) - C(u^n)].
\end{aligned}
\tag{3.42}$$

From a physicist's view point, the equations (3.33)-(3.40) express how to evaluate the average values within the space grids. The equation (3.42) is the semi-discrete time evolution part, which is not tightly coupled with the space value evaluation. For individual physical problems, the only information that need to provide when using this central scheme is the speed of information propagating (equation(3.38)) and a function to calculate $f(u)$ and $g(u)$ values (equation(3.36)) from u .

Such schemes are provided by CentPACK , [*Jorge Balb'as and Tadmor, 2006b*] , a software package that implements several central schemes for hyperbolic conservation laws. We have employed the two dimensional, second-order accurate, non-oscillatory semi-discrete central scheme in this numerical package as the base scheme in order to evolve the equation solutions for (3.27)-(3.32).

3.2.2 Special Topics About the Hall MHD Simulation

Since the Hall MHD simulation is very time consuming, we parallelized CentPACK via Message Passing Interface (MPI). The idea behind parallelizing this explicit scheme was to divide the computation domain into small sub-domains and replacing the boundary condition in CentPACK. For the computational nodes that calculated the sub-domains, which are not in the boundary of the computational domains, the values on the boundary were not evolved by the node itself. Instead, the values on boundary of these nodes were evolved by the neighboring nodes and passed in by MPI.

When calculating the MHD simulation via CentPACK, special consideration and work was still needed for the magnetic induction equation (3.19). Although the magnetic induction equation could be written into the conservative form as equation (3.27), it is not a conservative equation. Instead, the solenoidal constraint $\nabla \cdot \mathbf{B} = 0$ should be satisfied during the computation. In the nonlinear reconnection problem, we used a projection cleaner [Tóth, 2000] to correct the magnetic field and to satisfy the divergence free condition. Using the cleaner, the evolved magnetic field, that we denote by \mathbf{B}^* , was then reprojected (equation (3.44)) onto its divergence-free component by solving the Poisson equation (3.43), as follows:

$$\Delta\Phi = -\nabla \cdot \mathbf{B}^* \quad (3.43)$$

$$\mathbf{B}^{n+1} = \mathbf{B}^* + \nabla\Phi \quad (3.44)$$

We also used hyperresistivity in the simulation. The term in equation (3.31), with η_j as a coefficient, is the hyper-resistivity. This term is utilized to smooth the structure around the grid scale and is not strongly diffusive on longer scale lengths. The term is mainly numerical, however, electron viscosity can also bring this type of hyper-resistivity into the MHD model.

While calculating the terms in equation (3.31), we have approximated the high-order terms with higher order central finite differences. Term $(u_x)_{i,j}^{(n+1)}$ can be calculated as following, where the term $(u_x)_{i+1,j}^{(n)}$ is the n -th order derivative of u on x direction.

$$(u_x)_{i,j}^{(n+1)} = \frac{(u_x)_{i+1,j}^{(n)} - (u_x)_{i-1,j}^{(n)}}{\Delta x} \quad (3.45)$$

By applying the Hall MHD model into KT schemes [*Jorge Balb'as and Tadmor, 2006b*] package, we need to provide the whistler wave's group speed instead of the phase speed in section 3.1 (equation (3.24)) as the characteristic wave speed in the Hall MHD system. Because whistle wave propagates fastest along the magnetic field [*Hameiri et al., 2005*], we use the speed of the transverse wave along magnetic field as the fastest speed, ignoring the compressibility effect. After the electron inertia term has been added into the system, the group velocity and the phase velocity of the whistle wave decreases, but we are still using the whistler wave speed in our calculation. That's because we did not include the electron inertia in the time evolution steps. The electron inertia term calculation acts as a correcting step after each time evolution step. In each time evolution, the information or energy is still propagating as the Hall MHD system.

We notice that in the resistivity Hall MHD system, the group speed is increasing more sharply than phase speed when the wave number increases, which requires using more tiny time steps. Using CentPACK for our problems is still very computational resource-intensive.

In order to include the electron inertia term, we employed two methods. The first method used the time difference of the last time step value and the current time step value. The second method was the method recommended in [*Jones and Parker, 2003*]. The main ideas is as:

$$\frac{\partial \mathbf{B}'}{\partial t} = -\nabla \times \left(-\mathbf{v} \times \mathbf{B} + \frac{\mathbf{j} \times \mathbf{B}}{\rho} \right) \quad (3.46)$$

$$\mathbf{B}' = \mathbf{B} - \frac{1}{\rho} \frac{m_e}{m_i} \nabla^2 \mathbf{B} \quad (3.47)$$

The term \mathbf{B}' is the main parameter that evolves in time. After each step, after the new \mathbf{B}' has been calculated, we solve the linear equation (3.47) to obtain \mathbf{B} . Then the new \mathbf{B} is substituted into (3.46) in order to determine subsequent evolve the numerical schemes ahead. The first method is only doable when m_e/m_i is small. For the second method, we built a linear solver for equation (3.47) using the numerical package Portable Extensible Toolkit for Scientific computation (PETSc). For numerical reasons [Shay *et al.*, 2001], Shay used the following form of the equation in his simulation:

$$\frac{\partial \mathbf{B}'}{\partial t} = -\nabla \times \mathbf{E} + \eta_b \nabla^6 \begin{pmatrix} B_x \\ B_y \\ B_z \end{pmatrix} \quad (3.48)$$

$$\mathbf{B}' = \mathbf{B} - \frac{m_e}{m_i} \nabla^2 \mathbf{B} \quad (3.49)$$

$$\begin{pmatrix} E_x \\ E_y \\ E_z \end{pmatrix} = -\mathbf{v} \times \mathbf{B} + \eta_j \begin{pmatrix} \nabla^2 j_x \\ \nabla^2 j_y \\ \nabla^2 j_z \end{pmatrix} + \frac{\mathbf{j} \times \mathbf{B}'}{\rho}. \quad (3.50)$$

But these two forms of equations ignore some terms in the original formulation of the generalized Ohm's law [Ma and Bhattacharjee, 1999].

3.3 The Dispersion Relation Test

To test the validity of the proposed numerical scheme, we ran numerical tests. In the linear regime, we tested the dispersion relation of the system and quantitatively compared the results with the analytical solutions.

The basic numerical test is a test of the linear dispersion relationships. We launched a small sinusoidal oscillation with a wave length, λ , in a periodic box, then measured the frequency of the oscillation. Using the wave length and the frequency, we can tell whether or not the wave speed in the simulation is in agreement with the linear analytical prediction.

For the Hall MHD system, the linear analysis indicates that the wave mode corresponding to the lineally polarized Alfvén wave in the MHD is a circularly polarized wave, due to the fact that the magnetic field is frozen with electron flow in Hall MHD, instead of a plasma flow in the MHD system. Past researchers have named this wave as the whistler wave, or the circularly polarized Alfvén wave. Similar to the work of previous researchers [*Ma and Bhattacharjee, 2001; Toth et al., 2008*], we set the initial condition as the following:

$$\begin{aligned} \rho &= 1, & v_x &= 0, & v_y &= -\delta \cos(kx), & v_z &= \delta \sin(kx) \\ p &= 1, & B_x &= 1, & B_y &= \delta v_p \cos(kx), & B_z &= -\delta v_p \sin(kx), \end{aligned} \quad (3.51)$$

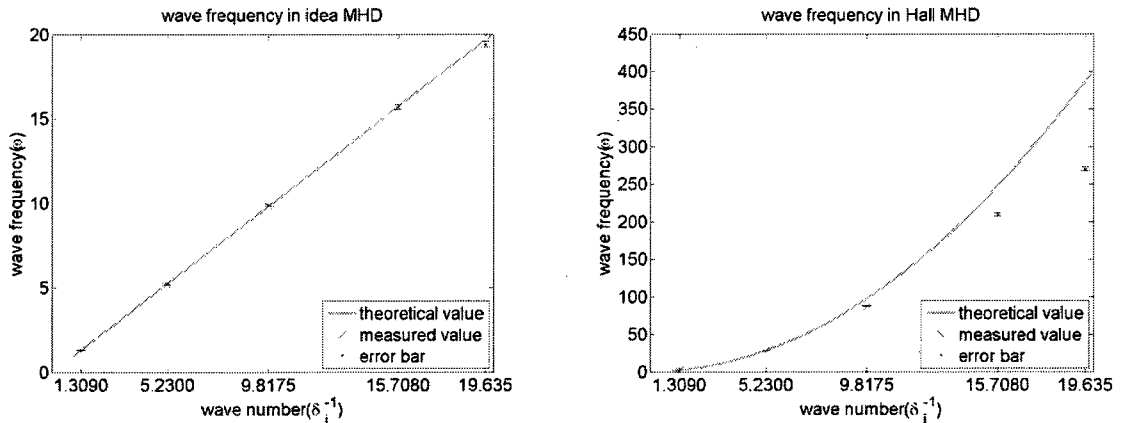
$$\text{while, } k = 2\pi m/x_L = 2\pi m/\lambda. \quad (3.52)$$

This circularly polarized wave will propagate in the x direction. From theoretical analyses, the density, the pressure, as well as the x components of the velocity and the magnetic field will not be perturbed by this oscillation in both Hall MHD and the standard MHD simulation. Therefore, in this numerical test, while a pure Alfvén mode wave is launched in the simulation domain, no other MHD waves, such as sonic or magnetosonic waves will be triggered. If we assign a perturbation of $\delta=0$, equation (3.51) represents a uniform plasma in an equilibrium state. We chose $\delta=10^{-5}$ in the

calculation. v_p is the phase speed calculated from the linear analysis, and x_L is the length of the simulation box, which is $9.6\delta_i$ in calculation. We tried several cases with $m=2,8,15,24,30$.

In the numerical test, the resolution was uniformly $\Delta x=0.05$. We used this resolution to determine at what resolution the dispersion relationship in the numerical result goes beyond the theoretical prediction. The linear analysis was accomplished in the three systems: the classic MHD, the Hall MHD without electron inertia, and the Hall MHD with electron inertia. The Hall MHD with electron inertia test ran with mass ratios of $1/300$ and $1/25$. The results obtained for these four systems are shown in Figure 3-1.

We find that the very high-speed whistler wave has the potential to cause some numerical trouble. Numerical results from standard MHD and the Hall MHD with electron inertia simulations agreed with the theoretical prediction until the wavelength gets down to about six grid sizes. At this resolution level Hall MHD tests without electron inertia displayed some discrepancies with theory. The results indicate that in Hall MHD simulations, spatial resolution is critical for numerical accuracy.



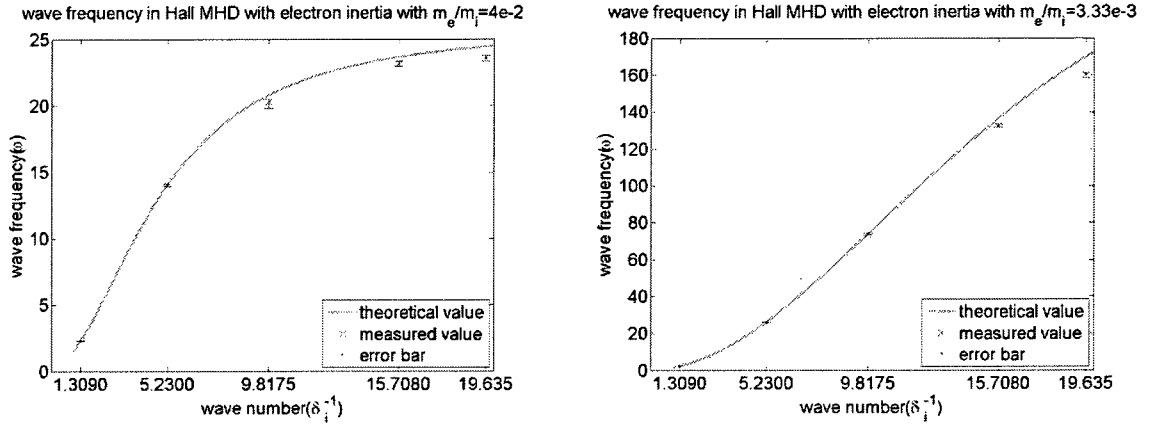


Figure 3-1: Dispersion relationship test result

Another important feature of the Hall MHD system with electron inertia is that the group speed of the whistler wave will approach zero when the wave number increases in the system. We will use this property of the electron inertia simulation to test whether the relationship between dispersion relationship and the current sheet length in reconnection phenomenon.

3.4 Hall MHD Reconnection Simulation

3.4.1 Initial condition and boundary condition

The goal of this thesis is to simulate the Hall MHD system without and with electron inertia. Hall MHD reconnection simulations have been extensively reported in the literature [*Huba and Rudakov, 2004; Ma and Bhattacharjee, 1996; 2001*]. Here, we present resistive Hall MHD reconnection cases first in order to validate our proposed numerical schemes. The initial condition and boundary condition discussed in this section are also used later in the Hall MHD simulations with electron inertia.

We focused on studying the reconnection in a perturbed equilibrium system, instead of in a reconnection caused by pressure from the boundary. We simulated a perturbed equilibrium problem in a two dimensional x - y plane, with different boundary conditions.

The equilibrium is a Harris current sheet without a guide field. The magnetic field, the density, and the pressure profile are given by the following:

$$B_x(y) = B_0 \tanh(y/\lambda) - \psi_0 y/L_y \cos(2\pi x/L_x) \sin(\pi y/L_y) \quad (3.53)$$

$$B_y = \psi_0 \cdot 2\pi/L_x \sin(2\pi x/L_x) \cos(\pi y/L_y) \quad (3.54)$$

$$n(y) = n_0 \operatorname{sech}^2(y/\lambda) + n_b \quad (3.55)$$

$$p(y) = \frac{1}{2} n(y). \quad (3.56)$$

These equations describe the background equilibrium plus the imposed perturbations. For initial equilibrium, the velocities are set to zero. In the above equations, parameter ψ_0 is the perturbation amplitude; and parameters B_0 and n_b are the background magnetic field and density, respectively. Parameters L_x and L_y are the system size in the x and y direction, respectively, and the half-width of the current sheet is determined by parameter λ .

As for the boundary condition, the GEM challenge has a periodic boundary in the x direction, and a conducting wall boundary in the y direction. We implemented the conduction wall boundary as described by Chacon [*Chacón*, 2004]. The main idea is to set the perpendicular current density to zero along the conduction wall boundary.

We also simulated open boundary problems [Daughton *et al.*, 2006] by assuming that the simulation box is in a region cut from a large background plasma. In the inflow direction, the open boundary is used to make the unperturbed background plasma flow into the simulation domain. In the out-flow direction, the open boundary is used to make the plasma that has passed through the reconnection diffusive region, flow out from the simulation domain without a reflection. The motivation for trying this boundary condition is to determine whether it can influence the extension of the current sheet and produce secondary instabilities as seen in the fully kinetic simulations.

For the inflow boundary, along the x direction, the pressure and the density of the plasma was fixed as the initial condition over time, so does B_x . B_z is calculated from $\partial B_z / \partial y = 0$, and B_y from the $\nabla \cdot \mathbf{B} = 0$ condition. As for the velocity components, v_x and v_z were set to zero and v_y was calculated from $\partial v_y / \partial y = 0$.

For the out-flow boundary, the pressure, the density, and the perpendicular velocity v_x were interpolated as follows:

$$u_{j+1} = 1.3u_j - 0.3u_{j-1}; \quad (3.57)$$

B_x is derived from the $\nabla \cdot \mathbf{B} = 0$ condition, and B_z , B_y , v_y , and v_z obey $\partial u / \partial y = 0$.

When the electron inertia is included, the components of \mathbf{B}' are assigned according to the same method that is applied for \mathbf{B} .

One should notice that the out-flow region in our simulation is not a supersonic super-Alfvén region. Therefore, a non-reflection boundary rarely gets rid of all possible reflection. Using the out-flow boundary described above, the reflection is still obvious at the beginning of the simulation, as seen in Figure 3-2.

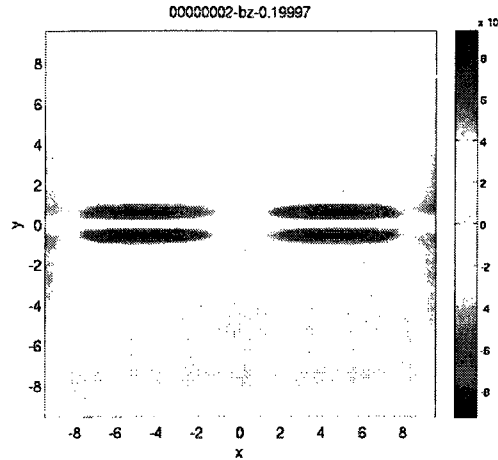


Figure 3-2: Out of plane magnetic field at very beginning stage of the simulation

3.4.2 Hall MHD Reconnection with Hyper-Resistivity

Resistivity Hall MHD simulations show an X configuration, a short current sheet [Ma and Bhattacharjee, 2001; Shay et al., 2001]. In this section, I outline our resistivity Hall MHD simulation result obtained using CentPACK. By comparing this result with other published results, we ensure the validity of our simulation method. In this section, details of the diffusion region in the resistive Hall MHD reconnection simulation are also discussed.

The numerical results presented here is the perturbed Harris sheet problem in an open boundary simulation system. Details of the governing equation, the initial and the boundary conditions can be found in sections 3.1 and 3.4.1 . The parameter λ was set to 0.5, the same as for the GEM challenge cases. The simulation cases had a system size of $9.8d_i \times 9.8d_i$ with 639×639 uniform grids. The grids in the simulation domain had a size of $0.03 d_i$.

We then looked deeply into the numerical result from a physical perspective in order to see whether it was in agreement with previous published results.

The reconnection rate of the out-of-plane electric field is displayed in Figure 3-3. The reconnection rate does not increase linearly. In the beginning, before approximately $18\omega_i^{-1}$, the reconnection rate increases gently. At this stage, the current sheet first becomes thin, then at approximately $18\omega_i^{-1}$, a short current sheet configuration is formed in the center of the simulation domain. Subsequently, after $18\omega_i^{-1}$, the reconnection rate begins to rise sharply until it reaches roughly $0.18 \sim 0.2$ at approximately $25.2\omega_i^{-1}$. At the same time, a singular current sheet region is formed in the center of the simulation domain. Following these two stages, the reconnection process reaches a quasi-steady state. The reconnection rate occurs at roughly 0.2 , while the current sheet has an X configuration, and does not change extensively. A very short and thin current sheet is found in the center of this X type configuration.

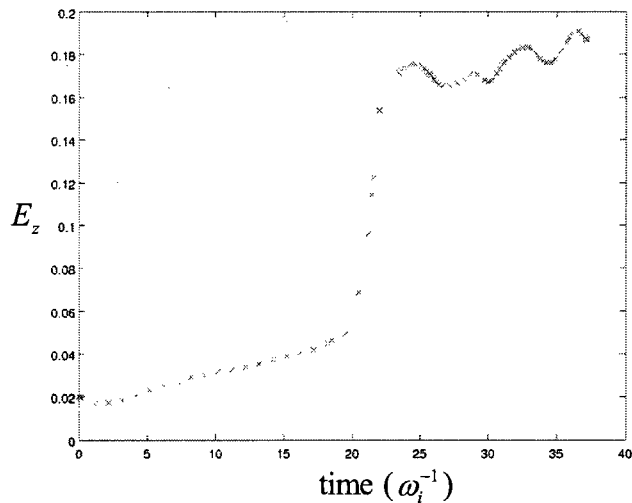


Figure 3-3: Reconnection rate for resistivity Hall MHD simulation

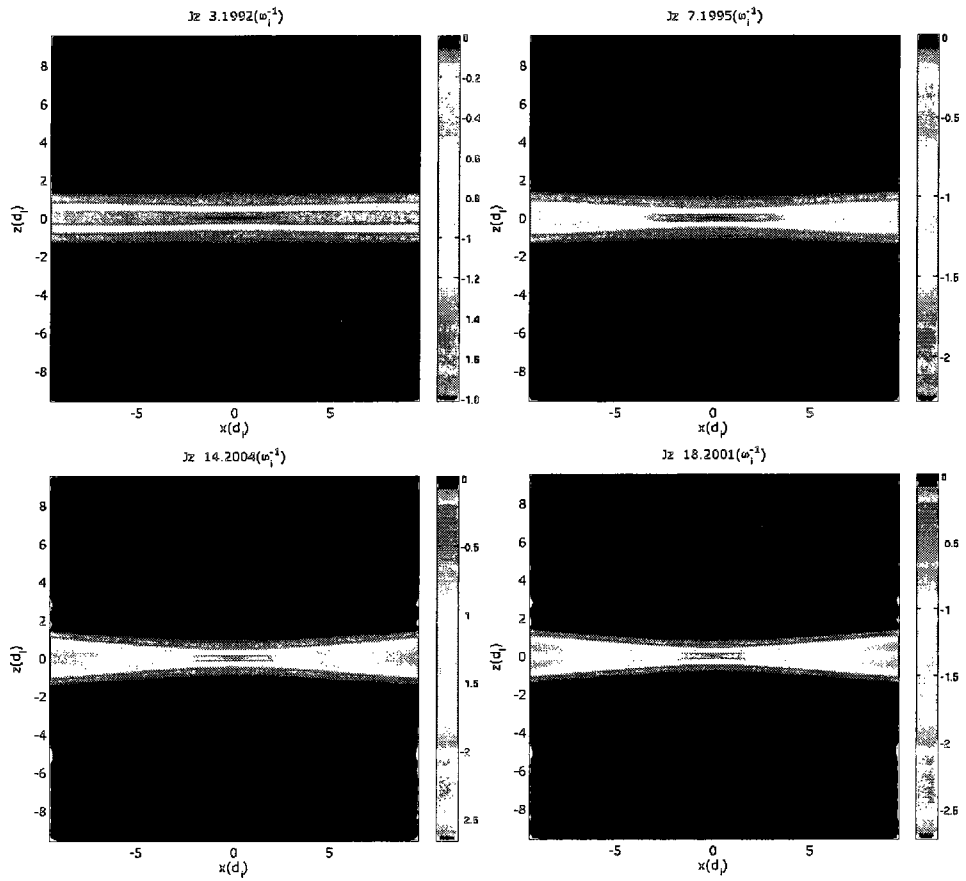


Figure 3-4: Current sheet's evolution when reconnection rate is increasing gently

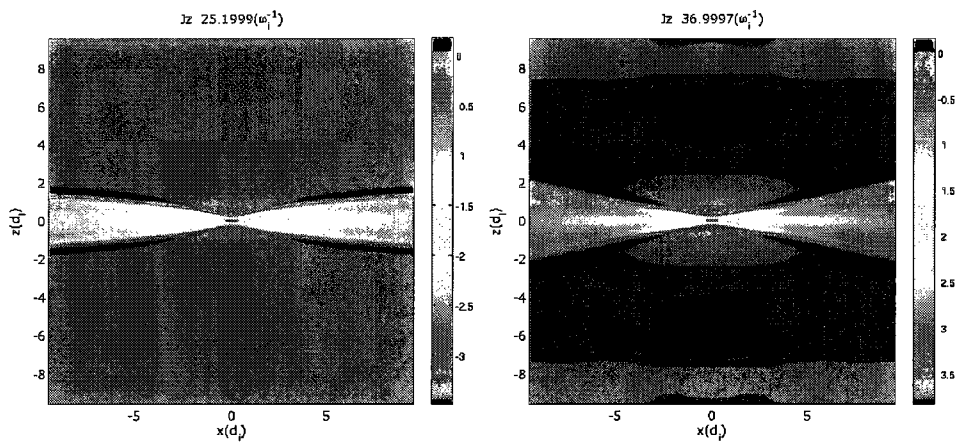


Figure 3-5: The current sheet shapes after quasi-steady state forms

After $25\omega_i^{-1}$, a diffusive region in the quasi-steady state is found. Once the X configuration forms, the current sheet has a very small size as seen in Figure 3-5 as well as Figure 3-6. Figure 3-6 shows the terms in generalized Ohm's law in the x and y direction. In the x direction, which is the out-flow direction, the current sheet or the electron diffusive region, where the $\eta\mathbf{j} + \eta_j\nabla^2\mathbf{j}$ is very large, has a length of approximately $1d_i$. In the y direction, the thickness of the current sheet is approximately $0.2d_i$, which is roughly four grids.

The out-plane absolute value of the electric field, E_z , is approximately 0.2, in agreement with the GEM challenge's conclusion, although, here, a different boundary condition was used. The out of plane electric field has a tiny strong area located in the electron diffusive region. From equation(3.4), it can be found that the space gradient of the out plane electric field will cause time variation of the in plane magnetic field. The system is only in a quasi-steady state. A time dependent variation is still occurring in the simulation domain, while the X type current sheet configuration does not change much.

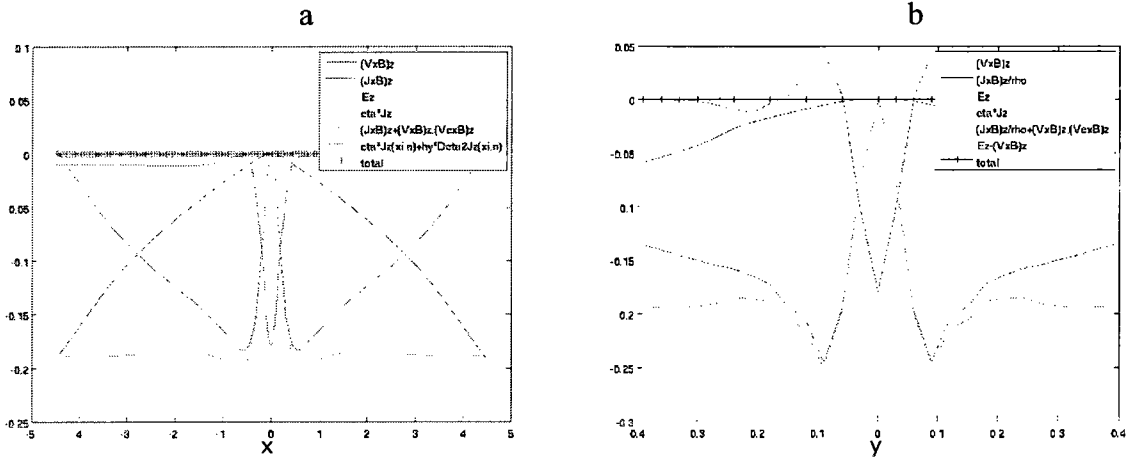


Figure 3-6: Terms in generalized Ohm's law at $33.6\omega_i^{-1}$

Figure 3-6 displays the terms in generalized Ohm's law on two lines, $x=0$ and $y=0$, surrounding the original point. The ion diffusive region also displays the two scale diffusive region feature, as predicted by the Hall MHD reconnection theory. For example, in Figure 3-6(a), $-(\mathbf{v} \times \mathbf{B})_z$ approaches E_z until $4.5d_i$. The ion diffusive region is the region inside $4.5d_i$. Outside of the ion diffusive region, $\mathbf{j} \times \mathbf{B} / \rho + \eta \mathbf{j} + \eta_j \nabla^2 \mathbf{j}$ is no longer important. Inside of the ion diffusive region, it is the Hall term $\mathbf{j} \times \mathbf{B} / \rho$ that makes the ions decouple with the magnetic field line. The electron diffusive region can be judged by the shape of the $(\mathbf{J} \times \mathbf{B})_z$ term, which is approximately $1d_i$ width in the outflow direction. Inside of the electron diffusive region, the term $\eta \mathbf{j} + \eta_j \nabla^2 \mathbf{j}$ becomes large. These terms make the electrons decouple with the magnetic field line.

For electron flow the following equation is applied:

$$\mathbf{j} = \nabla \times \mathbf{B} \Rightarrow \mathbf{j}_{(x,y)} = \hat{z} \times \nabla B_z. \quad (3.58)$$

The contour of B_z is the plane current flow pattern. The v_{ex} diagram (Figure 3-7 b) is in

agreement with the quadrupole feature of the B_z . As for the electron's flow in the x direction (Figure 3-7 a), the flow speed reaches a maximum before the electron leaves the diffusive region. So, before the electrons reach their maximum speed, they are accelerated by the reconnection electric field and turned in the out-flow direction by the Lorenz force. After the electrons reach their maximum speed, they are magnetized and once more coupled with the magnetic field. The fact that the electron diffusive region can be divided into regions of accelerating and magnetizing electrons is the core feature of the multiple scale electron diffusive regions. Therefore, the resistivity in Hall MHD simulation cases that have hyper-resistivity do have the so-called two-scale structure for the electron diffusive region, as outlined by [Karimabadi *et al.*, 2007]. Others performing Hall MHD simulations should also see this type of two-scale electron diffusive region in their simulations. However, here, for the first time, we present this type of two-scale electron diffusive region for a MHD simulation.

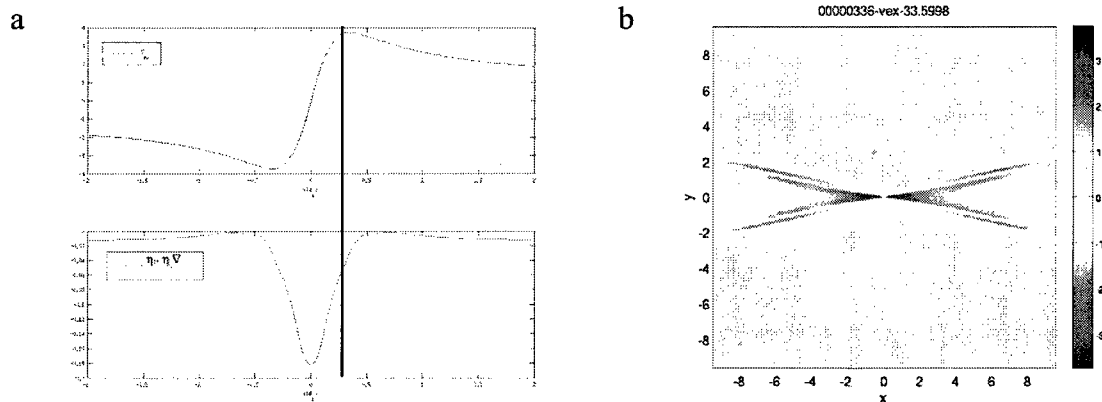


Figure 3-7: Electron's outflow at $33.6\omega_i^{-1}$

Hyper-resistivity is related to the electron's viscosity [Dieter Biskamp, 2000]. and is not a pure numerical term. However, in the resistivity Hall MHD simulation, the

hyper-resistivity numerical term is needed to diffuse the structures in the grid scale, while not being too diffusive at the large scale. Figure 3-8 shows a simulation case that we performed without the hyper-resistivity term. In this simulation, the current sheet had a depletion region in the center.

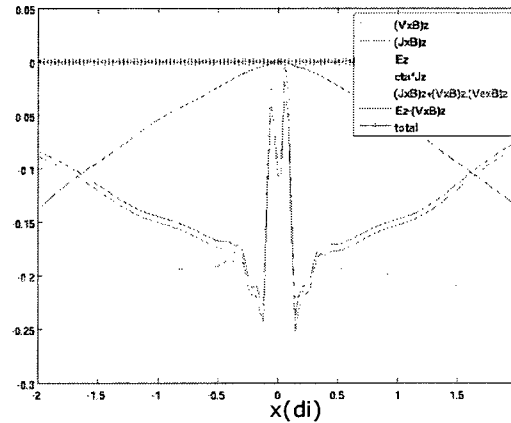


Figure 3-8: Terms in generalized Ohm's law in diffusive region

3.5 Hall MHD simulations including electron inertia

The numerical method of performing the resistivity Hall MHD simulation with electron inertia was discussed in section 3.2.2. In this section, I present our simulation results. We use mass ratios of 1/25 and 1/300, and different forms of the governing equations. We do not find any current sheet elongation and secondary instability in the simulations. In this respect, the results of Hall MHD simulations, with or without electron inertia, appear to be qualitatively different that the results of fully kinetic simulations.

In Case 1, the mass ratio was set at $1/25$. The governing equations regarding generalized Ohm's law are the following:

$$\frac{\partial \mathbf{B}'}{\partial t} = -\nabla \times \mathbf{E} + \eta_b \nabla^4 \mathbf{B}' \quad (3.59)$$

$$\mathbf{B}' = \left(1 - \frac{m_e}{m_i} \nabla^2\right) \mathbf{B} \quad (3.60)$$

$$\begin{pmatrix} E_x \\ E_y \\ E_z \end{pmatrix} = -\mathbf{v} \times \mathbf{B} + \eta_j \begin{pmatrix} \nabla^2 j_x \\ \nabla^2 j_y \\ \nabla^2 j_z \end{pmatrix} + \frac{\mathbf{j} \times \mathbf{B}'}{\rho}. \quad (3.61)$$

This form of equation has been used by the reference [Shay et al., 2001; Sullivan et al., 2009]. Equation (3.60) is a linear equation, and the linear operator $1 - \frac{m_e}{m_i} \nabla^2$, which is a matrix in the numerical method, does not change during the whole numerical simulation process. So we could use the SuperLU method via PETSC or Fast Fourier Transform (FFT) to solve this linear equation, which is very fast. As compared to equation (3.22), the term $1/\rho \cdot (\mathbf{v} \cdot \nabla) \mathbf{j}$ does not appear in this form of the equation. Reference [Dieter Biskamp, 2000] provided the explanation in page 208, which stated that in EMHD $1/\rho \cdot (\mathbf{v} \cdot \nabla) \mathbf{j}$ could be treated as $1/\rho \cdot (\mathbf{j} \cdot \nabla) \mathbf{j}$. Biskamp derived the EMHD equation as

$$\partial_t (\mathbf{B} - d_e^2 \nabla^2 \mathbf{B}) + \nabla \times [\mathbf{j} \times (\mathbf{B} - d_e^2 \nabla^2 \mathbf{B})] = \eta \nabla^2 \mathbf{B} - \eta_2 (\nabla^2)^2 \mathbf{B}. \quad (3.62)$$

Therefore, it appears that the above equation is not the only numerical choice.

As for the diffusive region's size, we found that for this case a thicker and a longer diffusive region was achieved in the center of the simulation domain (Figure 3-9, Figure 3-10), as compared to the Hall MHD case using hyper-resistivity (Figure 3-4).

The simulation also achieved a peak reconnection rate at 0.14, as seen in Figure 3-11, that was lower than the Hall MHD cases containing hyper-resistivity.

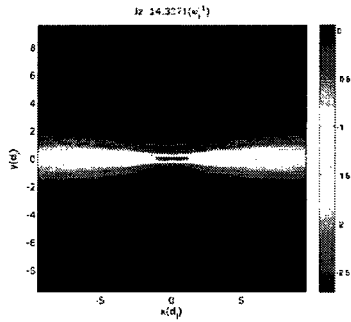


Figure 3-9: Out of plane current density in case 1 at 14.4

$$\omega_p^{-1}$$

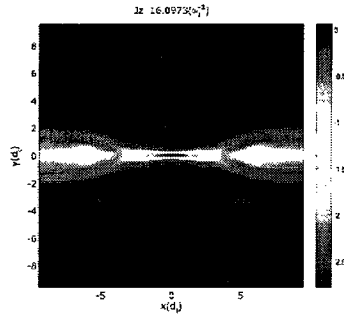


Figure 3-10: Out of plane current density in case 1 at 16.1

$$\omega_p^{-1}$$

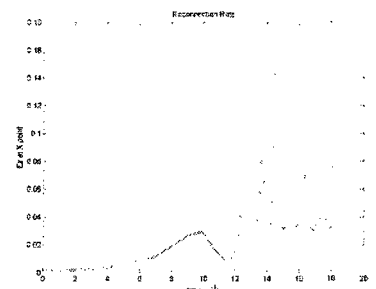


Figure 3-11: Reconnection rate for case 1

Except for the GEM challenge, most other simulation studies, use a smaller mass ratio, for example reference [Karimabadi *et al.*, 2007] has the mass ratio as 1/100, reference [Ma and Bhattacharjee, 1999] has the mass ratio as 1/200, and in reference [Rogers *et al.*, 2001] the simulation work is using mass ratio as 1/300. So we also would like to try different mass ratios in this study as what had been done by Shay in the GEM challenge [Shay *et al.*, 2001].

Case 2 utilized the same governing equations as Case 1, but Case 2 used a mass ratio of 1/300. For Case 2 we observed that the diffusive region becomes small. No obvious current sheet elongation and secondary instability were observed. As we discussed in section 3.2.2, the forms of the equations used in Cases 1 and 2 are missing several terms and ignore some of the physical effects. We have attempted to add these missing terms into the simulation to test whether they might make a difference.

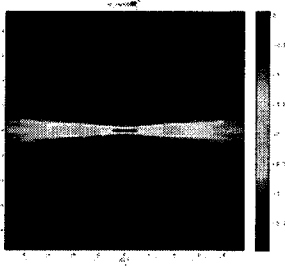


Figure 3-12: Out of plane current density in case 2 at 14.0

ω_i^{-1}

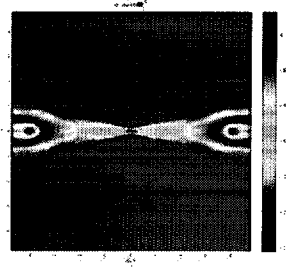


Figure 3-13: Out of plane current density in case 2 at 19.4

ω_i^{-1}

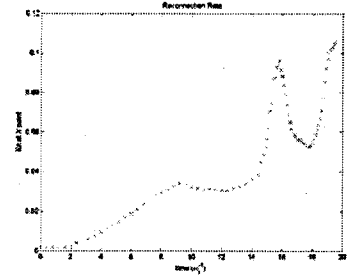


Figure 3-14: Reconnection rate for case 2

For Case 3 we used a mass ratio of $1/300$. However, the governing equation was as follows:

$$\frac{\partial \mathbf{B}'}{\partial t} = -\nabla \times \mathbf{E} \quad (3.63)$$

$$\mathbf{B}' = \left(1 - \frac{m_e}{m_i} \nabla^2\right) \mathbf{B} \quad (3.64)$$

$$\begin{pmatrix} E_x \\ E_y \\ E_z \end{pmatrix} = -\mathbf{v} \times \mathbf{B} + \eta_j \begin{pmatrix} \nabla^2 j_x \\ \nabla^2 j_y \\ \nabla^2 j_z \end{pmatrix} + \frac{\mathbf{j} \times \mathbf{B}}{\rho} + \frac{m_e}{m_i} \frac{1}{\rho} \left(v_x \frac{\partial}{\partial x} + v_y \frac{\partial}{\partial y} + v_z \frac{\partial}{\partial z} \right) \begin{pmatrix} j_x \\ j_y \\ j_z \end{pmatrix}. \quad (3.65)$$

The main difference for this case and for Case 2 was the $\frac{\mathbf{j} \times \mathbf{B}}{\rho}$ and $\frac{1}{\rho}(\mathbf{v} \cdot \nabla) \mathbf{j}$ terms. These forms of the equations are the same as reference [Jones and Parker, 2003] except the term $\frac{1}{\rho}(\mathbf{v} \cdot \nabla) \mathbf{j}$. We also did not observe the current sheet elongation and secondary instability.

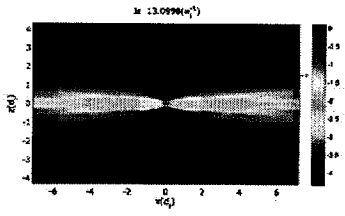


Figure 3-15: Out of plane current density in case 3 at 13.1

ω_i^{-1}

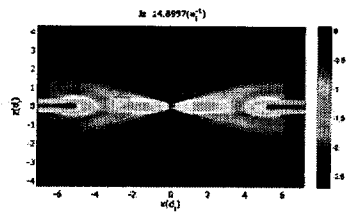


Figure 3-16: Out of plane current density in case 3 at 14.8

ω_i^{-1}

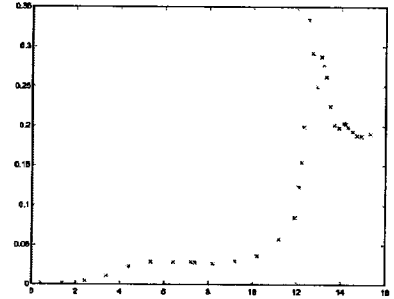


Figure 3-17: Reconnection rate in case 3

Case 4 used the following governing equation:

$$\frac{\partial \mathbf{B}'}{\partial t} = -\nabla \times \mathbf{E} \quad (3.66)$$

$$\mathbf{B}' = \left(1 - \frac{1}{\rho} \frac{m_e}{m_i} \nabla^2\right) \mathbf{B} \quad (3.67)$$

$$\begin{pmatrix} E_x \\ E_y \\ E_z \end{pmatrix} = -\mathbf{v} \times \mathbf{B} + \eta_j \begin{pmatrix} \nabla^2 j_x \\ \nabla^2 j_y \\ \nabla^2 j_z \end{pmatrix} + \frac{\mathbf{j} \times \mathbf{B}}{\rho} + \frac{m_e}{m_i} \frac{1}{\rho} \left(v_x \frac{\partial}{\partial x} + v_y \frac{\partial}{\partial y} + v_z \frac{\partial}{\partial z} \right) \begin{pmatrix} j_x \\ j_y \\ j_z \end{pmatrix}. \quad (3.68)$$

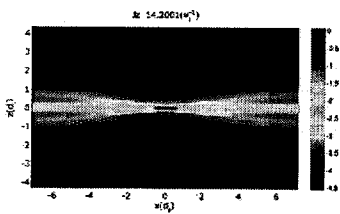


Figure 3-18: Out of plane current density in case 4 at 14.2

ω_i^{-1}

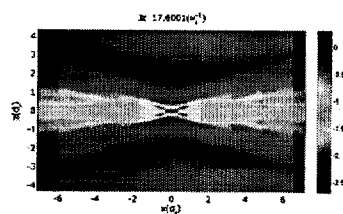


Figure 3-19: Out of plane current density in case 4 at

$17.6 \omega_i^{-1}$

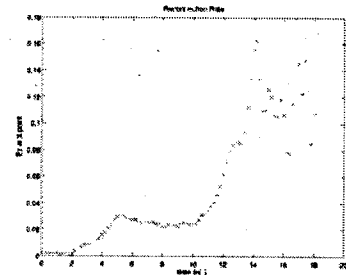


Figure 3-20: Reconnection rate in case 4

Numerically, this case was more expensive than the previous three cases since equation (3.67) cannot be solved using the Super LU method. For Case 4, we did not observe current sheet elongation and secondary instability.

3.6 Conclusion

Our results indicate that central schemes provide a simple and robust approach for approximating the solutions of non-classical MHD models with complex wave structures. In the linear regime, the dispersion relationship test shows agreement with theoretical results. In the nonlinear regime, the Hall MHD via CentPACK gives simulation results in qualitative agreement with other Hall MHD simulation studies. Here, we also report a two scale electron diffusive region in the Hall MHD simulation, as seen also in PIC simulations.

We utilize different forms of the electron inertia governing equation, which included forms of equations that are the same or that included more effects as found in comparable references [*Jones and Parker, 2003; Shay et al., 2001*]. Thus far, our electron inertial simulations have not shown an apparent current elongation or a secondary instability. Because we did not completely include all terms attributable to electron inertia in the generalized Ohm's law (at least not as many as used by [*Ma and Bhattacharjee, 1999*]), we cannot conclude that the electron inertia term cannot produce some current elongation and secondary instability. It is very likely that the absence of elongation and secondary instabilities may be due to the modest system size of these simulations, as the very recent work [*Huang et al., 2010*] appears to show.

CentPACK has been shown to be successful in MHD reconnection simulation. From the numerical view point, this is evidence that the numerical package build via central schemes like CentPACK can be used as a universal tool for hyperbolic partial differential equations, even for such complex problem as Hall MHD reconnection. This type of approach can decouple the numerical scheme programming and the physical model. So the parallelization of the numerical schemes and grids distribution can be done independent to the physical model. Because the basic numerical schemes have been proved to be valid in my above simulation work, I think we can begin applying modern parallelization method and AMR (Adaptive mesh refinement) method in this kind of numerical packages. Then physicists will have a simple and powerful tool for their numerical simulation work involving hyperbolic partial differential equations.

References

- Arp, O., D. Block, A. Piel, and A. Melzer (2004), Dust Coulomb Balls: Three-Dimensional Plasma Crystals, *Physical Review Letters*, 93(16), 165004.
- Kahlert, H., and M. Bonitz (2010), How Spherical Plasma Crystals Form, *Physical Review Letters*, 104(1), 015001.
- Balb'as, J., and E. Tadmor (2006a), Nonoscillatory Central Schemes for One- and Two-Dimensional Magnetohydrodynamics Equations. II: High-Order SemiDiscrete Schemes, *SIAM J. Sci. Comput.*, 28, 533-560.
- Balb'as, J., and E. Tadmor (2006b), CentPack, edited, online at <http://www.cscamm.umd.edu/centpack/software>.
- Balb'as, J., E. Tadmor, and C. C. Wu (2004), Non-oscillatory central schemes for one- and two-dimensional MHD equations: I, *Journal of Computational Physics*, 201, 261-285.
- Bessho, N., and A. Bhattacharjee (2007), Fast collisionless reconnection in electron-positron plasmas, *Physics of Plasmas*, 14(5), 056503-+.
- Bhattacharjee, A., Y.-M. Huang, H. Yang, and B. Rogers (2009), Fast reconnection in high-Lundquist-number plasmas due to the plasmoid instability, *Physics of Plasmas*, 16(11), 112102-112105.
- Birn, J., et al. (2001), Geospace Environmental Modeling (GEM) magnetic reconnection challenge, *Journal of Geophysical Research*, 106, 3715-3720.
- Biskamp, D. (1997), Collisional and collisionless magnetic reconnection, *Physics of Plasmas*, 4, 1964-1968.
- Biskamp, D. (2000), *Magnetic Reconnection in Plasmas*, Cambridge University Press
- Biskamp, D., E. Schwarz, and J. F. Drake (1995), Ion-Controlled Collisionless Magnetic Reconnection, *Physical Review Letters*, 75(21), 3850.
- Chacón, L. (2004), A non-staggered, conservative, finite-volume scheme for 3D implicit extended magnetohydrodynamics in curvilinear geometries, *Computer Physics Communications*, 163(3), 143-171.
- Chen, Z., M. Y. Yu, and H. Luo (2005), Molecular Dynamics Simulation of Dust Clusters in Plasmas, *Physica Scripta*, 71, 638.
- Culbert B. Laney (1998), *Computational Gasdynamics*, Cambridge University Press.
- Chu, J. H., and L. I (1994), Direct observation of Coulomb crystals and liquids in strongly coupled rf dusty plasmas, *Phys. Rev. Lett.*, 72(25), 4009-4012.
- Daniel H. E. D. (2001), The Phonon Wake Behind a Charge Moving Relative to a 2D Plasma Crystal, *Physica Scripta Online*, T89, 63-66.

- Daughton, W., J. Scudder, and H. Karimabadi (2006), Fully kinetic simulations of undriven magnetic reconnection with open boundary conditions, *Physics of Plasmas*, 13, 2101.
- Daughton, W., V. Roytershteyn, B. J. Albright, H. Karimabadi, L. Yin, and K. J. Bowers (2009), Transition from collisional to kinetic regimes in large-scale reconnection layers, *Physical Review Letters*, 103(6), 065004.
- Del Zanna, L. a. B., N. and Londrillo, P. (2003), An Efficient Shock-Capturing Central-type Scheme for Multidimensional relativistic flows II, *Astronomy and Astrophysics*, 400, 397--413.
- Deng, X. H., and H. Matsumoto (2001), Rapid magnetic reconnection in the Earth's magnetosphere mediated by whistler waves, *Nature*, 410, 557-560.
- Deng, X. H., et al. (2009), Dynamics and waves near multiple magnetic null points in reconnection diffusion region, *J. Geophys. Res.*, 114(A7), A07216.
- Dubin, D. H. E. (2000), The phonon wake behind a charge moving relative to a two-dimensional plasma crystal, *Physics of Plasma*, 7(10), 3895.
- Dubin, D. H. E., and T. M. O'Neil (1999), Trapped nonneutral plasmas, liquids, and crystals (the thermal equilibrium states), *Reviews of Modern Physics*, 71(1), 87.
- Fujimoto, K. (2006), Time evolution of the electron diffusion region and the reconnection rate in fully kinetic and large system, *Physics of Plasmas*, 13, 2904.
- Gottlieb, S., C.-W. Shu, and E. Tadmor (2001), Strong Stability-Preserving High-Order Time Discretization Methods, *SIAM Rev.*, 43(1), 89-112.
- Gurnett, D. A., and A. Bhattacharjee (2005), *Introduction to Plasma Physics with Space and Laboratory Applications*, Cambridge University Press.
- Hameiri, E., A. Ishizawa, and A. Ishida (2005), Waves in the Hall-magnetohydrodynamics model, *Physics of Plasmas*, 12(7), 072109-+.
- Harten, A., B. Engquist, S. Osher, and S. R. Chakravarthy (1987), Uniformly high order accurate essentially non-oscillatory schemes, III, *Journal of Computational Physics*, 71(2), 231-303.
- Havnes, O., T. Aslaksen, T. W. Hartquist, F. M. F. Li, G. E. Morfill, and T. Nitter (1995), Probing the Properties of Planetary Ring Dust by the Observation of Mach Cones, *JOURNAL OF GEOPHYSICAL RESEARCH*, 100(A2), 4.
- Havnes, O., F. Li, Melands, F., T. Aslaksen, T. W. Hartquist, G. E. Morfill, T. Nitter, and V. Tsytovich (1996), Diagnostic of dusty plasma conditions by the observation of Mach cones caused by dust acoustic waves, *Journal of Vacuum Science & Technology A: Vacuum, Surfaces, and Films*, 14(2), 525-528.
- Horányi, M., T. W. Hartquist, O. Havnes, D. A. Mendis, and G. E. Morfill (2004), Dusty plasma effects in Saturn's magnetosphere, *Rev. Geophys.*, 42(4), RG4002.

- Hua, J.-J., Y.-H. Liu, M.-F. Ye, L. Wang, and Z.-H. Zhang (2003), Structural and Dynamical Analysis of a Two-Dimensional Dusty Plasma Lattice, *Chinese Phys. Lett.*, 20(1), 155.
- Huang, Y.-M., and A. Bhattacharjee (2010), Scaling laws of resistive magnetohydrodynamic reconnection in the high-Lundquist-number, plasmoid-unstable regime, *Physics of Plasmas*, 17(6), 062104-062108.
- Huang, Y.-M., A. Bhattacharjee, and B. Sullivan (2010), Onset of Fast Reconnection in Hall Magnetohydrodynamics Mediated by the Plasmoid Instability.
- Huba, J. D., and L. I. Rudakov (2004), Hall Magnetic Reconnection Rate, *Physical Review Letters*, 93(17), 175003.
- Ivanov, Y., A. Melzer, and eacute (2009), Modes of three-dimensional dust crystals in dusty plasmas, *Physical Review E*, 79(3), 036402.
- Jiang, K., et al (2009), Mach cones in a three-dimensional complex plasma, *EPL*, 85(4).
- Jones, S. T., and S. E. Parker (2003), Including electron inertia without advancing electron flow, *J. Comput. Phys.*, 191(1), 322--327.
- Kahlert, H., and M. Bonitz (2010), How Spherical Plasma Crystals Form, *Physical Review Letters*, 104(1), 015001.
- Karimabadi, H., W. Daughton, and J. Scudder (2007), Multi-scale structure of the electron diffusion region, *Geophysical Research Letters*, 34, 13104.
- Konopka, U., G. E. Morfill, and L. Ratke (2000), Measurement of the Interaction Potential of Microspheres in the Sheath of a rf Discharge, *Physical Review Letters*, 84(5), 891.
- Kurganova, A., and E. Tadmor (2000), New High-Resolution Central Schemes for Nonlinear Conservation Laws and Convection 盼 iffusion Equations, *Journal of Computational Physics*, 160, 241-282.
- Levy, D., G. Puppo, and G. Russo (2002), A Fourth-Order Central WENO Scheme for Multidimensional Hyperbolic Systems of Conservation Laws, *SIAM Journal on Scientific Computing*, 24(2), 480-506.
- Loureiro, N. F., A. A. Schekochihin, and S. C. Cowley (2007), Instability of current sheets and formation of plasmoid chains, *Physics of Plasmas*, 14(10), 100703-100704.
- Loureiro, N. F., D. A. Uzdensky, A. A. Schekochihin, S. C. Cowley, and T. A. Yousef (2009), Turbulent magnetic reconnection in two dimensions, *Monthly Notices of the Royal Astronomical Society: Letters*, 399(1), L146-L150.
- Ma, Z. W., and A. Bhattacharjee (1996), Fast impulsive reconnection and current sheet intensification due to electron pressure gradients in semi-collisional plasmas, *Geophysical Research Letters*, 23, 1673-1676.

- Ma, Z. W., and A. Bhattacharjee (1999), Sudden disruption of a thin current sheet in collisionless Hall magnetohydrodynamics due to secondary tearing and coalescence instabilities, *Geophysical Research Letters*, 26(22), 3337-3340.
- Ma, Z. W., and A. Bhattacharjee (2001), Hall magnetohydrodynamic reconnection: The Geospace Environment Modeling challenge, *Journal of Geophysics Research*, 106, 3773-3782.
- Ma, Z. W., and A. Bhattacharjee (2002), Molecular dynamics simulation of Mach cones in two-dimensional Yukawa crystals, *Physics of Plasma*, 9(8), 3349.
- Mann, I. (2008), Interplanetary medium - A dusty plasma, *Advances in Space Research*, 41(1), 160-167.
- Melzer, A., S. Nunomura, D. Samsonov, Z. W. Ma, and J. Goree (2000), Laser-excited Mach cones in a dusty plasma crystal, *Physical Review E*, 62(3), 4162.
- Morfill, G. E., and H. Thomas (1996), PLASMA CRYSTAL, *Journal of Vacuum Science & Technology A-Vacuum Surfaces & Films*, 14(2), 490-495.
- Nosenko, V., J. Goree, Z. W. Ma, and A. Piel (2002), Observation of Shear-Wave Mach Cones in a 2D Dusty-Plasma Crystal, *Physical Review Letters*, 88(13), 135001.
- Peeters, F. M., and X. Wu (1987), Wigner crystal of a screened-Coulomb-interaction colloidal system in two dimensions, *Physical Review A*, 35(7), 3109.
- Petschek, H. E. (1964), Magnetic Field Annihilation, *The Physics of Solar Flares, Proceedings of the AAS-NASA Symposium held 28-30 October, 1963 at the Goddard Space Flight Center*.
- Pieper, J. B., J. Goree, and R. A. Quinn (1996), Three-dimensional structure in a crystallized dusty plasma, *Physical Review E*, 54(5), 5636--5640.
- Quinn, R. A., and J. Goree (2000), Experimental investigation of particle heating in a strongly coupled dusty plasma, *Physics of Plasmas*, 7(10), 3904-3911.
- Quinn, R. A., C. Cui, J. Goree, J. B. Pieper, H. Thomas, and G. E. Morfill (1996), Structural analysis of a Coulomb lattice in a dusty plasma, *Physical Review E*, 53(3), R2049--R2052.
- Ren, Y., M. Yamada, S. Gerhardt, H. Ji, R. Kulsrud, and A. Kuritsyn (2005), Experimental Verification of the Hall Effect during Magnetic Reconnection in a Laboratory Plasma, *Physical Review Letters*, 95(5), 055003.
- Rogers, B. N., R. E. Denton, J. F. Drake, and M. A. Shay (2001), Role of Dispersive Waves in Collisionless Magnetic Reconnection, *Physical Review Letters*, 87(19), 195004.
- Samsonov, D., J. Goree, Z. W. Ma, A. Bhattacharjee, H. M. Thomas, and G. E. Morfill (1999), Mach Cones in a Coulomb Lattice and a Dusty Plasma, *Physical Review Letters*, 83(18), 3649.

- Samtany, R., N. F. Loureiro, D. A. Uzdensky, A. A. Schekochihin, and S. C. Cowley (2009), Formation of Plasmoid Chains in Magnetic Reconnection, *Physical Review Letters*, 103(10), 105004.
- Schiffer, J. P. (2002), Melting of Crystalline Confined Plasmas, *Physical Review Letters*, 88(20), 205003.
- Schweigert, I. V., V. A. Schweigert, A. Melzer, and A. Piel (2000), Melting of dust plasma crystals with defects, *Physical Review E*, 62(1), 1238.
- Shay, M. A., J. F. Drake, B. N. Rogers, and R. E. Denton (1999), The scaling of collisionless, magnetic reconnection for large systems, *Geophysical Research Letters*, 26(14), 2163.
- Shay, M. A., J. F. Drake, B. N. Rogers, and R. E. Denton (2001), Alfvénic collisionless magnetic reconnection and the Hall term, *Journal of Geophysical Research*, 106, 3759-3772.
- Shepherd, L. S., and P. A. Cassak (2010), Comparison of Secondary Islands in Collisional Reconnection to Hall Reconnection, *Physical Review Letters*, 105(1), 015004.
- Shukla, P. K. (2001), A survey of dusty plasma physics, *Physics of Plasmas*, 8(5), 1791-1803.
- Sullivan, B. P., A. Bhattacharjee, and Y.-M. Huang (2009), Extension of the electron dissipation region in collisionless Hall magnetohydrodynamics reconnection, *Physics of Plasmas*, 16(10), 102111-102111.
- Thomas, H. M., and et al. (2008), Complex plasma laboratory PK-3 Plus on the International Space Station, *New Journal of Physics*, 10(3), 033036.
- Toth, G., Y. Ma, and T. I. Gombosi (2008), Hall magnetohydrodynamics on block-adaptive grids, *Journal of Computational Physics*, 227, 6967-6984.
- Tóth, G. (2000), The [backward difference]·B=0 Constraint in Shock-Capturing Magnetohydrodynamics Codes, *Journal of Computational Physics*, 161(2), 605-652.
- Totsuji, H., T. Ogawa, C. Totsuji, and K. Tsuruta (2005), Structure of spherical Yukawa clusters: A model for dust particles in dusty plasmas in an isotropic environment, *Physical Review E (Statistical, Nonlinear, and Soft Matter Physics)*, 72(3), 036406.
- van Leer, B. (1979), Towards the ultimate conservative difference scheme. V. A second-order sequel to Godunov's method, *Journal of Computational Physics*, 32(1), 101-136.
- Verheest, F. (1996), Waves and instabilities in dusty space plasmas, *Space Science Reviews*, 77(3), 267-302.
- Wahlund, J. E., et al. (2009), Detection of dusty plasma near the E-ring of Saturn, *Planetary and Space Science*, 57(14-15), 1795-1806.
- Wang, X., A. Bhattacharjee, and S. Hu (2001), Longitudinal and Transverse Waves in Yukawa Crystals, *Physical Review Letters*, 86(12), 2569.